Theses and Dissertations

2015

Exploring Initial Condition Effects on Variable Acceleration Rayleigh Taylor Instability using Impilicit Large Eddy Simulations

Denis Aslangil
Lehigh University

Follow this and additional works at: http://preserve.lehigh.edu/etd

Part of the Mechanical Engineering Commons

Exploring Initial Condition Effects on Variable Acceleration Rayleigh Taylor Instability using Implicit Large Eddy Simulations

by

Denis Aslangil

A Thesis

Presented to the Graduate and Research Committee

of Lehigh University

in Candidacy for the Degree of

Master of Science

in

Mechanical Engineering & Mechanics

Lehigh University

August 2015

This thesis is accepted and approved in partial fulfillment of the requirements
for the Master of Science in Mechanical Engineering.

Exploring Initial Condition Effects on Variable Acceleration Rayleigh Taylor

Instability using Implicit Large Eddy Simulations

Denis Aslangil

_____

Date Approved

_____

Prof. Arindam Banerjee
Thesis Advisor
Department of Mechanical Engineering & Mechanics
Lehigh University

_____

Prof. Gary Harlow
Department Chair Person
Department of Mechanical Engineering & Mechanics
Lehigh University

ACKNOWLEDGEMENTS

TABLE OF CONTENTS

LIST OF FIGURES

ABSTRACT

Rayleigh Taylor Instability (RTI) occurs at the interface between a light fluid and a heavy fluid due to the gravitational impact and is commonly observed in several natural and engineering processes like internal confinement fusion (ICF), Type Ia supernova formation and in turbulent combustion processes. Traditionally, RTI has been studied under a constant acceleration frame-work, primarily due to the need of understanding the instability as it occurs in climate and geologic dynamics as well as in deep sea oceanic currents. However, there exists several applications like blast waves, ICF and stellar dynamics where gravitational variability alters the dynamics of the RTI induced mixing process. It is thus important to understand the late-time evolution of RTI under variable acceleration and in cases where the acceleration changes sign.

Our primary motivation is to investigate of the effects of initial conditions on self-similar evolution to turbulence of RTI under variable acceleration histories. Incompressible, three dimensional RTI is modeled using a massively parallel high resolution code, MOBILE which uses an Implicit Large Eddy Simulation (ILES) technique. In the current work, four different initial conditions are investigated to understand the effect of spectral bandwidth and spectral index on the late time evolution of the instability as it undergoes multiple acceleration reversals. Our goal is to identify the similarities and differences between the Rayleigh–Taylor turbulence and the more general forms of quasi-stationary turbulence. We will discuss on our results, include low order metrics like, growth constant, molecular mixing parameter and second order moments and anisotropy tensors.

NOMENCLATURE

SYMBOL	DESCRIPTION
g	Acceleration
B_{ii}	Anisotropy tensors
A_t	Atwood number
α_b	Bubbles growth rate
h_b	Bubble height
θ	Global atomic mix parameter
ρ_H	Heavy fluid density field
h_{tot}:	Height of total mixing layer
Z	Interface displacement
ρ_L	Light fluid density field
$<u_3c>$	Mass flux
k	Mode number
$<cc>$	Scalar variance
α_s	Spikes growth rate
h_s	Spikes height
$<u_3u_3>$	Vertical component of velocity variance

ABBREVIATIONS	DESCRIPTION
ADA	Accel-Decel-Accel
AS	Annular Spectra
BB	Broadband
CG	Constant Gravity
DNS	Direct Numerical Simulation
Eq.	Equation
Fig.	Figure
ILES	Implicit Large Eddy Simulation
ICF	Inertial Confinement Fusion
ICs	Initial Conditions
LES	Large Eddy Simulations
LEM	Linear Electric Motor
RTI/RT	Rayleigh Taylor Instability
TVB	Total Variation Bounded

1. INTRODUCTION

Rayleigh-Taylor [1, 2] instability (RT/RTI) occurs at a perturbed interface between a light fluid (ρ_L) and a heavy fluid (ρ_H) due to the acceleration caused by gravity. The perturbations are infinitesimal and are characterized by height, h_0, and wavelength, $\lambda = 2\pi/k$. The instability commonly occurs in various natural and industrial flows like combustion and chemical reactor processes [3, 4], pollutant dispersion [5], internal confinement fusion (ICF) [6, 7], and in stellar dynamics such as Type Ia supernova explosions [8-11]. For small enough initial perturbations ($h \ll 1/k$), mixing width grows exponentially as [12]

$$h(t) = h_0 \cosh(\Gamma t), \tag{1}$$

where $\Gamma = \sqrt{A_t g k}$ is defined as the classical growth rate. Here, A_t, the Atwood Number, is the non-dimensional density difference between the two fluids and is defined as: $A_t = (\rho_H - \rho_L)/(\rho_H + \rho_L)$, which can range between values of 0 and 1 [13]. At late-times ($h > 1/k$), the growth saturates and the evolution of the mix-width can be defined based on dimensional analysis as [14, 15]

$$h_{b,s} = \alpha_{b,s} A_t g t^2, \tag{2}$$

where h_b is the bubble height which signifies the light fluid's penetration into the heavier one, and h_s is the spike height which signifies the heavy fluid's penetration into the lighter one (subscript b indicating bubbles and s indicating spikes) seen in Figure 1; g is the acceleration; t is the time; and $\alpha_{b,s}$ is the growth rate parameter. At low A_t numbers, the mix is symmetric as

11

bubbles grow similar to spikes resulting in $\alpha_b \approx \alpha_s$. As the density difference between the two fluids increases, the symmetry at the interface breaks, and spikes penetrate faster through bubbles; this results in $\alpha_s > \alpha_b$ with $\alpha_s \rightarrow \frac{1}{2}$ as $A_t \rightarrow 1$. In this study, a moderate A_t number ($A_t = 0.5$), where the symmetry is no longer prevented at the interface, has been investigated.
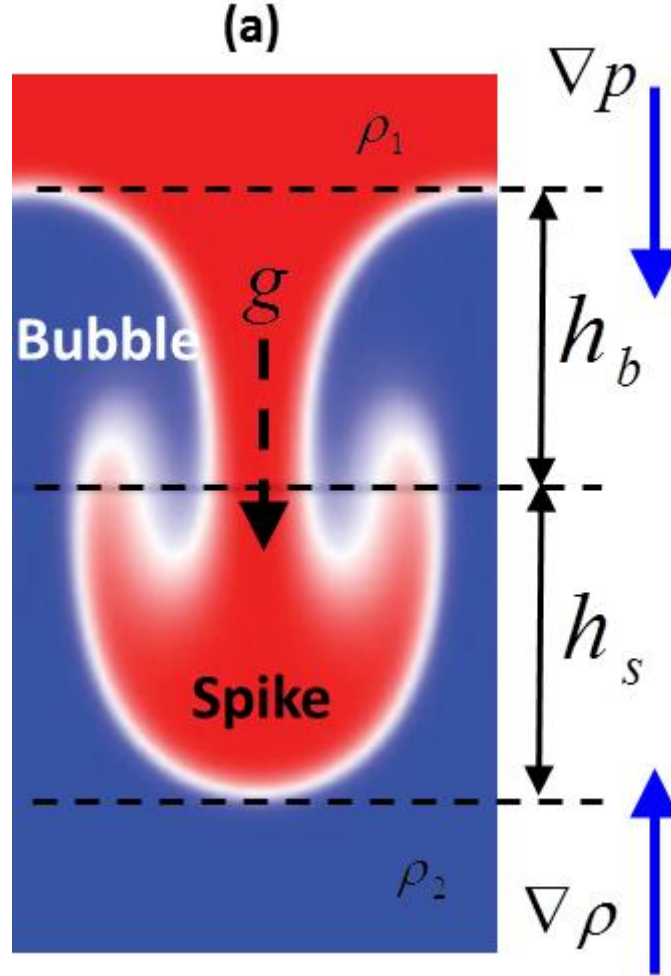
Figure 1. Bubble and spike evolution of the single mode RTI [16].

Eq. (2) shows that the mixing width grows quadratically with time and reaches a self-similar length scale ($A_t gt^2$) at late-times where the flow has lost memory of its initial conditions (ICs) [12]. However, there is no universal value for this growth parameter, and it has been

demonstrated in computations to be strongly dependent on the ICs [12, 17, 18]. The need to investigate the ICs' effects on the evolution of conventional RTI (under constant acceleration) has appeared due to the differences between the calculated alpha values from numerical and experimental studies in which the latter systematically reported larger alpha values [17]. The discrepancy between experiments and numerical studies was related with the presence of the long wave-length in the experiments, an aspect that was not represented in earlier numerical studies [19].

Ramaprabhu and Andrews [17] ran simulations to study initial-condition effects on conventional RTI with ICs obtained from experiments and demonstrated that simulations initialized with long wave-length perturbations, as evidenced in most experiments, reported larger alpha values. These values were in good agreement with the results from experiments [20, 21]. Meanwhile, Dimonte et al. [22] in their α-Group study, investigated RTI with different available numerical codes using the Implicit Large Eddy Simulation (ILES) and Large Eddy Simulation (LES) techniques and imposed initial perturbations with short wave-lengths, where perturbations had energy only in their high mode-numbers (32-64) at a grid resolution of 256×256×512. In the current work, a representative case similar to the α-Group study was used as IC1; the original attempt was to limit the asymptotic self-similar evolution of the shorter wavenumbers' progress by the nonlinear coupling of saturated modes in order to reduce ICs effects on the RT problem. The α-Group study reported smaller values of α_b ~0.025±0.003that contrasted relevant experimental results, which were explained as a consequence of fine-scale dilution and/or presence of long wave-length perturbations in the experiments.

1.1. RTI with Variable Acceleration

Compared to RTI with constant acceleration, RTI with varying acceleration histories that include acceleration reversals is a relatively uncharted and mostly ignored problem. Several practical applications that includes blast waves, ICF capsules, and those of Type Ia supernova formations [23-25] involve RTI driven by a time-varying acceleration history. To date, there is only one experiment (that uses miscible fluids) [26] and only a couple of simulation efforts [13, 24, 25] that explore RTI effects under variable acceleration. The effect of initial conditions on the late-time evolution of a time varying RTI is largely unexplored and is a focus of this thesis. We explore the role of initial conditions on RTI undergoing multiple acceleration reversals and compare it to the classical case of RTI undergoing a constant acceleration. Acceleration is reversed multiple times; the flow starts with an initially destabilizing acceleration (Accel phase, $g>0$) followed by a first reversal to a stabilizing acceleration (Deccel phase $g<0$). This is then followed by a second reversal to the Accel phase ($g>0$). Such a time varying RTI problem is called the ADA or accel-deccel-accel problem [23, 25]. The first acceleration reversal is selected arbitrarily and is sufficiently early in time such that the flow has reached self-similarity (as in Eq. 2). In the second case, acceleration is kept constant as in conventional RTI and is used for comparison purposes. Computational studies on RTI with constant acceleration by Ramabraphu et al. [18] and Banerjee and Andrews [12] have investigated the effect of spectral bandwidth, spectral shape, and discrete banded spectra; our choice of ICs closely matches ICs used by these studies. This allows us to verify and validate our constant gravity simulations while exploring new physical insights with the ADA acceleration history.

RTI with variable acceleration histories has been investigated using the Linear Electric Motor (LEM) experiment [23, 26]; however, the experiments used immiscible fluids at Atwood numbers 0.48 [23] and 0.22 [26]. In their 1996 experimental study, Dimonte and Schneider [26] investigated four different acceleration histories that included a constant-, increasing-, decreasing-, and impulsive- accelerations generated using the LEM. They reported that increasing acceleration ($dg/dt>0$) leads to faster growth of h_b than constant and in decreasing acceleration ($dg/dt>0$) histories. A subsequent publication by Dimonte et al. [23] used the gradual accel-decel-accel profile (not a step function) in which they observed shredding, i.e. decomposition of the modes of dominant bubbles and spikes during the deceleration phase. This shredding led to an increase in molecular mixing leading to a delay in the initiation of the growth of the mixing layer upon the second reacceleration.

Recently, Ramaprabhu et al. [25] simulated RTI using a similar accel-deccel-accel profile to the Dimonte experiment [23] for both a single wavenumber for Atwood numbers 0.15 and 0.9, as well as a spectrum of wavenumbers with Atwood number 0.5. The results were obtained using a massively parallel ILES code, MOBILE, and were in good agreement with reported experimental results. The study concluded that swapping acceleration rapidly changes the structure of the flow; decelerating the system induces a rapid increase in the rate of molecular mixing and increases the isotropy within the region, whereas re-accelerating recovers the self-similar RT anisotropic mixing problem. Livescu et al. [13] and Livescu and Wei [24] ran direct numerical simulations (DNS) of RTI with acceleration reversal and similarly reported that after acceleration reversal the molecular mixing increases within the flow. Their preliminary results also showed that the large-scale anisotropy decreases within the inner region of the mixing layer; although, interestingly, at the edge regions of the mixing layer, small-scale anisotropy increases

related to buoyancy forces. The reported physics occurring on the edge regions of the mixing layer encourage the idea that ICs would continue to play an important role on the flow evolution even during deceleration and re-acceleration periods.

The primary motivation of the current work is to investigate the effects of ICs similar to those used in the traditional (constant acceleration) RTI studies to evaluate self-similar evolution to turbulence of RTI under variable acceleration histories. Three different ICs were carefully imposed on the RT problem under variable acceleration histories to investigate the effects of: (a) spectral bandwidth and (b) spectral shape on RT dynamics. The objective was to investigate the mechanisms that are common to the accelerating and re-accelerating period and to unravel how ICs affect the flow evolution under acceleration reversals. In this study global RTI metrics, the mean concentration, the mixing layer growth rate, the molecular mixing parameter, second order moments, and anisotropy tensors are presented with second order moments' their spatial profiles as well. The thesis is organized as follows: in § 2 the numerical method and problem setup are described. The results of the self-similar analyses and effects of ICs for two different acceleration histories are given in § 3. Finally, we summarize our findings in § 4.

2. NUMERICAL METHOD AND PROBLEM SET

2.1.   MOBILE

MOBILE is an incompressible Navier-Stokes solver for three dimensional, incompressible flows with density based finite volume approach [27-29]. Mass and momentum equations are solved based on the fractional step method by separating the components as hyperbolic (advective transport), parabolic (scalar diffusion and viscous dissipation) and elliptic (pressure and velocity correction). The nonlinear velocity-based advection algorithm is monotonic and converges between 2nd and 3rd orders. The parabolic operators automatically choose a semi-implicit or explicit method regarding computational efficiency. The projection of an intermediate velocity field onto the nearest divergence-free vector field exactly conserves discrete angular momentum, though not discrete linear momentum using the well-known Hodge decomposition. The pressure Poisson equation, an output of the projection, was solved by means of full multi-grid acceleration. For parallelization the MPI protocol was applied. A macro language interpreter, being transparent to the parallelization, was used for post processing of flow fields, calculating derived quantities, reducing them to concise statistics, and visualization. The interpreter syntax saved for the initial serial/parallel distribution of memory allocated for interpreted variables.

2.2.   Advection Algorithm

The fractional step method is implemented in MOBILE, where the three-dimensional (3D) problem is split into sequences of *x-y-z-z-y-x* one dimensional update instructions, following the approach of Strang [30] to improve temporal orders of convergence. These one-dimensional advection sub-problems are total variation bounded (TVB), where even without properly solving the gradients, the unphysical oscillations are eliminated and the full 3D numerical stability is maintained. To achieve higher spatial order, the left and right states of the Riemann problem are modified by using piecewise polynomial reconstruction of the spatial field, and Godunov's exact solution is used to solve the local Riemann problem across cell faces.

Instead of using the most obvious linear gradient:

$$m_{i-1} = \frac{\varphi_i - \varphi_{i-2}}{2\Delta x}$$
(3)

to choose for a linear reconstruction in the cell at x_{i-1}, MOBILE, by default, uses a higher order estimate of the gradient, which is given in Eq.4. The fluxed volume per unit area, $u_{i-1/2} \Delta t$, is used to reconstruct the gradient and serves as a weighting that tends the gradient toward a central difference over the cell face.

$$m_{i-1} = (1 + \frac{u_{i-1/2}\Delta t}{\Delta x}) \frac{\varphi_{i-1} - \varphi_{i-2}}{3} + (2 - \frac{u_{i-1/2}\Delta t}{\Delta x}) \frac{\varphi_i - \varphi_{i-1}}{3}$$
(4)

The domain is carefully divided into staggered grids, which allows the code to accurately calculate scalar fluxes with only one elliptic pressure solver by storing scalar quantities at cell centers and storing face-normal velocities on their respective faces; however, each momentum component of the fluxes are calculated conservatively on each of the displaced grids. According to local velocity gradients, the method, which is applied in the flow, is not spatially independent, and a van-Leer-type limiter interpolates the flux between low and high order. The error scales is

18
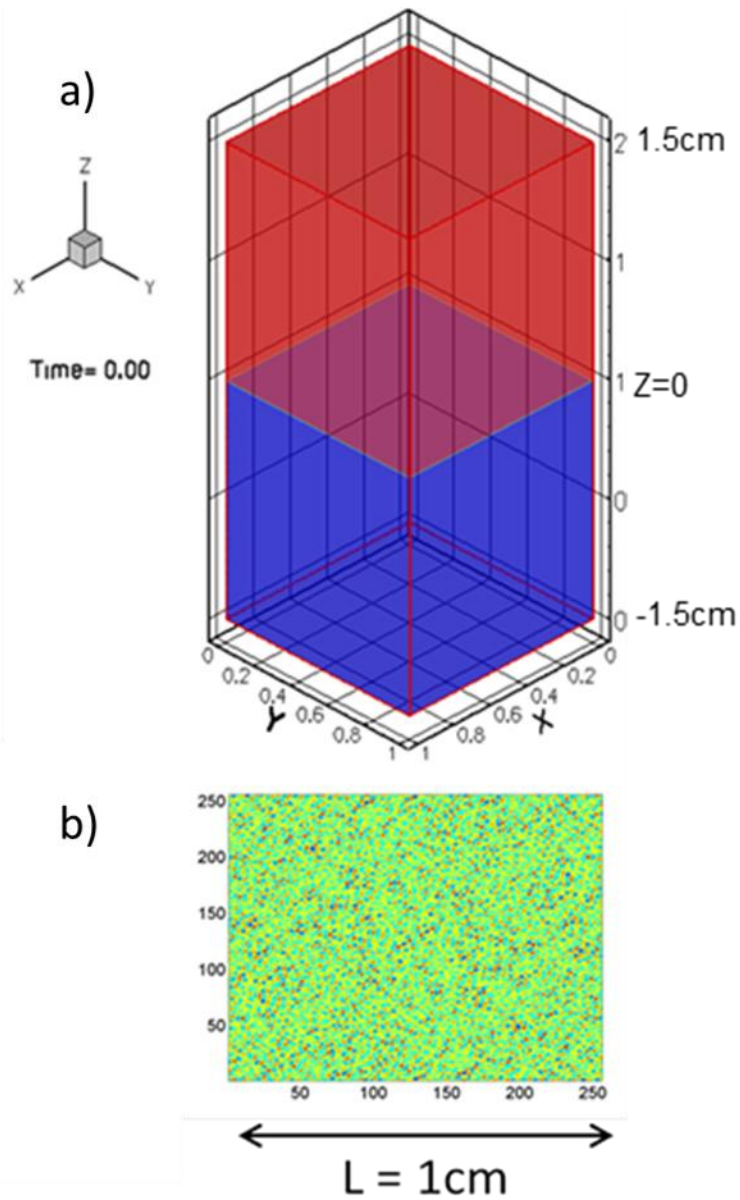
Figure 2. (a) Schematic of computational domain used in simulations. The box size is $1 \times 1 \times 3$ cm (in the x-, y- and z- directions) with densities $\rho_1 = 3.0$ g/cm^3 (red: heavy), $\rho_2 = 1.0$ g/cm^3 (blue: light). (b) Contour plot of initial amplitudes at center-plane ($z = 0$); the amplitudes correspond to annular narrowband ICs with energy in modes 32-64.

approximately observed as $O(\Delta x^n)$ where n is between 2 and 3 by empirical tests, even though the stencil retains the spatial compactness of the standard stencil for second order.

The current work used the ILES technique, in which small-scale dissipation is modeled numerically. The method eliminates the need for an explicit sub-grid filter with tunable coefficients and has been validated in a large number of flow conditions. Additionally, the monotonicity of the solution is preserved in RT problems by the ILES technique, even with discontinuous sharp flow features such as shocks or material interfaces. MOBILE, in use of ILES mode, produces dissipative spectra consistent with the expected $E(k) \sim k^{-3}$ scaling, which is compatible with observed values in experiments [31, 32] and Direct Numerical Simulation (DNS) calculations [33, 34]. Considering that the ILES technique is not grid independent—because of its ability in resolution to represent aspects of the physical problem and effects of the initial conditions—we made a conscious choice to use MOBILE in ILES mode.

2.3. Problem Setup

In the current work, a three dimensional computational domain was used, as seen in Figure 2, and has $L \times L \times 3L$ dimensions in the *x-, y-* and *z-* directions, respectively, with $L = 1.0$ cm. The gravity was applied in the *z*-direction $(0, 0, g_z)$, and the interface of the fluids was at $z = 0$. In the *x-* and *y-* directions, periodic boundary conditions were used while zero-flux conditions were imposed in the *z*-direction. The Atwood number of 0.5 was chosen by assigning densities for the lighter fluid, $\rho_L = 1.0$ g/cm^3, and for the heavier fluid, $\rho_H = 3.0$ g/cm^3. The initial conditions were created as perturbations h_0 (x,y) and then they were switched to volume fraction fluctuations as follows [12]:

$$
\begin{aligned}
f_1(x,\,y) &= 1 + h_0(x,\,y)/\Delta, &\quad \text{for } h_0 < 0 \\
f_1(x,\,y) &= h_0(x,\,y)/\Delta, &\quad \text{for } h_0 > 0
\end{aligned}
\tag{5}
$$

where Δ is the width of the computational cell. The resolutions were selected as 256×256×768 in

x-, y- and z-directions, respectively, for all simulations.

The simulations were run on an HPz820 workstation at Lehigh University. A total of

twelve cores were used for the runs. Each of these simulations required 8 GB of RAM, and the

run-times on the PC averaged around 1-2 weeks per simulation. The validation of the MOBILE

code and convergence study was reported in Ramaprabhu et al. [25], where increasing resolution

causes little change on simulations.

2.3.1. Initial Conditions

The simulations were initialized to understand the effects of spectral index and spectral

bandwidth (see Fig. 3). That all simulations have the same initial energy is a crucial property for

comparing the initial condition effects. The perturbation function (Eq.6) [22] is used to initialize

the simulations (detailed information and the FORTRAN script of the ICs can be found in

Appendix A):

$$
\begin{aligned}
h(x,\,y) = \sum_{k_x,k_y} &a_k \cos(k_x x)\cos(k_y y) + b_k \cos(k_x x)\sin(k_y y) + \\
&c_k \sin(k_x x)\cos(k_y y) + d_k \sin(k_x x)\sin(k_y y)
\end{aligned}
\tag{6}
$$

where $k = \sqrt{k_x^2 + k_y^2}$ and the a_k, b_k c_k and d_k are Fourier amplitude coefficients. The spectral

amplitudes are chosen randomly but give the same r.m.s. amplitude of $\sim 3.15 \times 10^{-4}$ L for all

simulations and the energy density spectrum is calculated as:

21

$$\frac{\overline{h_0'^2}}{2} = \int_{k_{min}}^{k_{max}} E_{h0}(k)dk$$

(7)
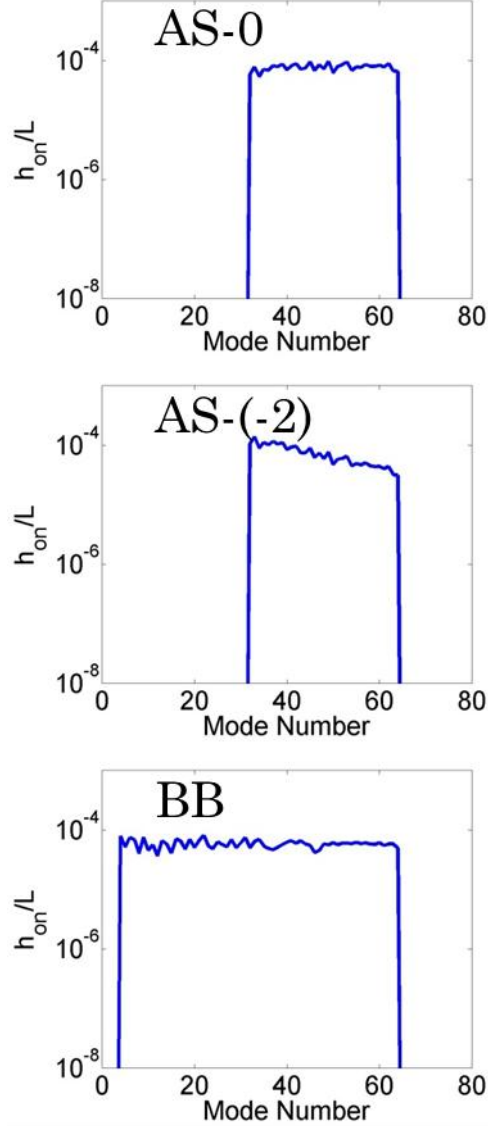
Figure 3. Azimuthally averaged initial conditions for all simulation cases listed in Table 1 with a root mean square amplitude of 3.15×10^{-4} L (where domain size is $L \times L \times L$)

The initial condition 1 (IC 1) with mode numbers ($n = kL/2\pi$) 32-64 and spectral index (p_s) of 0 was selected as a base case and used for comparison purposes; this was also used in the "alpha-group" study [22]. The simulation initialized with IC1, which is also our narrow band case, was named AS (0). IC 2, referred to as AS (-2), had modes 32-64, and a spectral index value of -2, indicating higher energy in large wavelengths. IC 3 with spectral index 0 differed in terms of mode numbers and had a minimum value of 4. It was meant to investigate the effect of spectral bandwidth, which has greater ability to represent the ICs are seen in experiments, and is called BB. Finally, the case abbreviated as CG [CG-AS (0)] represents simulation under constant gravity initialized with the corresponding IC. Table 1 summarizes the simulations presented in this study:

Table 1. List of simulations in the current work

IC #	IC type	Modes	SI	Acceleration History
IC1	CG-AS (0)	32-64	0	Constant Gravity
IC2	AS (0)	32-64	0	A-D-A
IC3	AS (-2)	32-64	-2	A-D-A
IC4	BB	4-64	0	A-D-A

2.3.2. Acceleration Histories

Variable acceleration histories are important in validating mix problems [23] and have been previously studied by various researchers [13, 23, 25, 35-37]. In the current work, we use a time varying acceleration-deceleration-acceleration (ADA) history on the evolution of RT instability with the ICs listed in Table 1. The results are compared with constant gravity (CG) computations which use similar initial conditions, thereby providing us a direct one-to-one comparison.

The ADA profile is chosen to represent the acceleration profile of the Linear Electric Motor experimental study [23] and also is similar with the profile used in the Ramaprabhu et al. [25] study. Ramaprabhu et al.[25] used three different acceleration values: 2cm/s^2, 4cm/s^2 and 8cm/s^2; whereas, here, g_0 was selected as 4cm/s^2 to study ICs effects on defined ADA profile. The acceleration profile was approximated by the Heaviside (step) function as:

$$g_z = g_0\{1 - H(t-2)(2) + H(t-4)(2)\} \tag{8}$$

The *H(t-2)* step function represents the time scale for the first swapping of acceleration; *H(t-2)* is assigned a value of 0 for *t<2s* and a value of 1 for *t≥2*. The *H(t-4)* step function represents a second swapping of the acceleration and acts similarly. The system switches from a mixing problem to a partial de-mixing problem at $t = 2s$ ($Z = 8cm$) and returns to a classic RT problem by re-swapping acceleration at $t = 4s$ ($Z = 16cm$). All simulations stopped when the bubble height reached 1.35 cm in order to prevent boundary conditions in *z-* direction. Otherwise, simulations were continued until time $t = 7.2s$.

Corresponding velocities are derived as [23, 25, 38]:

$$U(t) = \int_0^t g(t')dt', \tag{9}$$

By integrating velocity once, we obtain the related length-scale interface displacement $Z(t)$ as [25]:

$$Z(t) = \int_0^t U(t'')dt'' = \int_0^t \int_0^{t''} g(t')dt'dt'', \tag{10}$$

where t' and t'' are integrands and arbitrary. It is well-known that bubble and spike heights and Z (t) vary quadratically with respect to time [25, 38]; hence, $h_{b,s}$ will grow linearly with the length scale Z (t) as $h_{b,s} = 2\alpha_{b,s}A_t Z(t)$ for constant acceleration histories. Acceleration, velocity, and length scale $Z(t)$ profiles versus time can be seen in Fig.4.
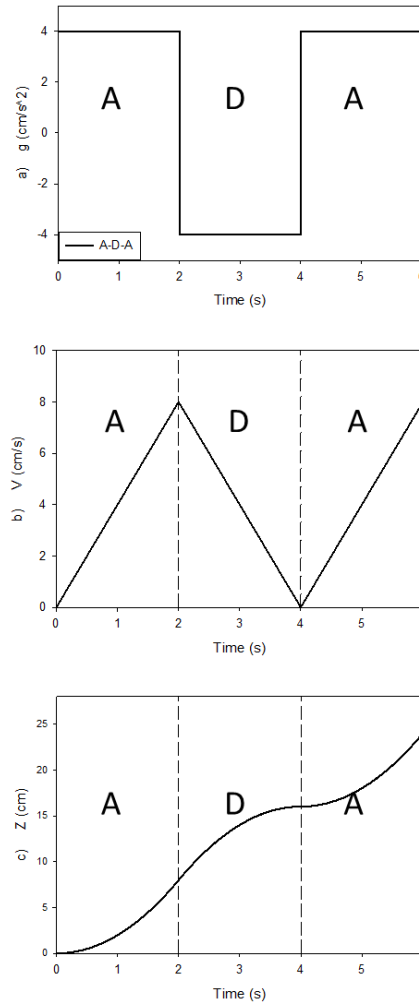
Figure 4. Profiles of (a) acceleration, (b) velocity, and, (c) Z(t) length-scale for the accel-decel-accel (A-D-A) acceleration history.

3. RESULTS

In this section, we discuss IC effects on the self-similar evolution of global RTI parameters that include the growth-rate parameter ($\alpha_{b,s}$) and the global atomic mix parameter (θ) under ADA acceleration history. As in the case of other turbulent flows, self-similarity is an important concept in RTI as the attainment of self-similarity simplifies the analyses. Self- similar analysis also provides a deeper understanding on the RTI turbulence structure. These detailed data sets can be used for modeling RTI and similar physical problems such as material mixing of two fluids under a framework of variable acceleration. Previous studies have identified two physical approaches to reach self-similarity in multimode RTI with constant acceleration [21, 22]. In the first approach, which is known as *bubble merger*, two or more bubbles may merge and form larger structures as a part of a continuous and repetitive process during the evolution of the RT mixing layer [18, 22]. In contrast, the concept of *bubble competition* involves amplification and saturation of long wavelengths and they lead the flow. Haan [39] postulated that the transition to nonlinearity is triggered when the sum of modal amplitudes reaches ~σ/k, implying that individual modes may become non-linear even before their amplitudes reach the non-linear threshold (σ) due to the interaction of adjacent modes.

Constant acceleration RTI studies [12, 16-18] have shown that it is possible to change the time to non-linearity, i.e. it is possible to saturate modes at earlier or later times by changing the initial amplitude which results in changes to the growth rate of the mixing layer. In this study, the growth rate of the mixing layer width ($\alpha_{b,s}$) is calculated by using Ristorcelli and Clark's [40] definition:

$$\alpha_{b,s} = \frac{\dot{h}_{b,s}^2}{4A_t g h_{b,s}} \tag{11}$$

whose self-similar analysis for early time concluded with a quadratic form of the mix-width:

$$h(t;, C_0, h_0) = \frac{1}{4} Ag C_0 t^2 + \sqrt{Ag C_0 h_0} \, t + h_0 \tag{12}$$

which determines the early time evolution of half width of the mixing layer (for low A numbers, $h_b \sim h_s \sim h$). In eq.12, h_0 accounts for initial condition effects during the linear growth period; for late time, the equation turns into the well-known empirical form: $h(t;, C_0) = \frac{1}{4} C_0 Ag t^2$, which exhibits the growth rate: $\alpha = \frac{1}{4} C_0$. Ristorcelli and Clark [40] also indicated that the asymptotic growth rate (which can be calculated using Eq.11) is not universal. Moreover, the flow is not self-similar in a conventional sense and depends on initial conditions.

A computational technique based on Implicit Large Eddy Simulations (ILES) has been used to study ICs effects on RTI [12, 17, 18]. Using the RTI-3D code [41], the majority of these studies showed that the ICs with longer wavelengths lead to a faster growth of the mixing layer width, indicating values of the growth constant similar to that reported in experiments [31, 42]. In the present study, we initialized our simulations with ICs similar to Banerjee and Andrews [12]. This allowed us to compare the ADA results with their [12] constant gravity results and also offered a mode of a secondary validation for the MOBILE code. In addition to the broad-band effect, Banerjee and Andrews also reported that their simulation, which was initialized with a negative spectral index value (the representative case being NB-(-2) in this study), received alpha values between those measured from narrow band and broad-band cases. We observed similar behavior through MOBILE during the first acceleration period, which will be discussed subsequently.

27

Recent studies by Ramaprabhu et al. [25] investigated RTI under a variable acceleration ADA profile. The simulation was initialized with multi-mode annular ICs similar to those used in the α-Group study [22]. The corresponding case used for comparison in our study was AS-0. In fig.4, the volume fraction contours of the density field are shown for AS (0) by means of (i)
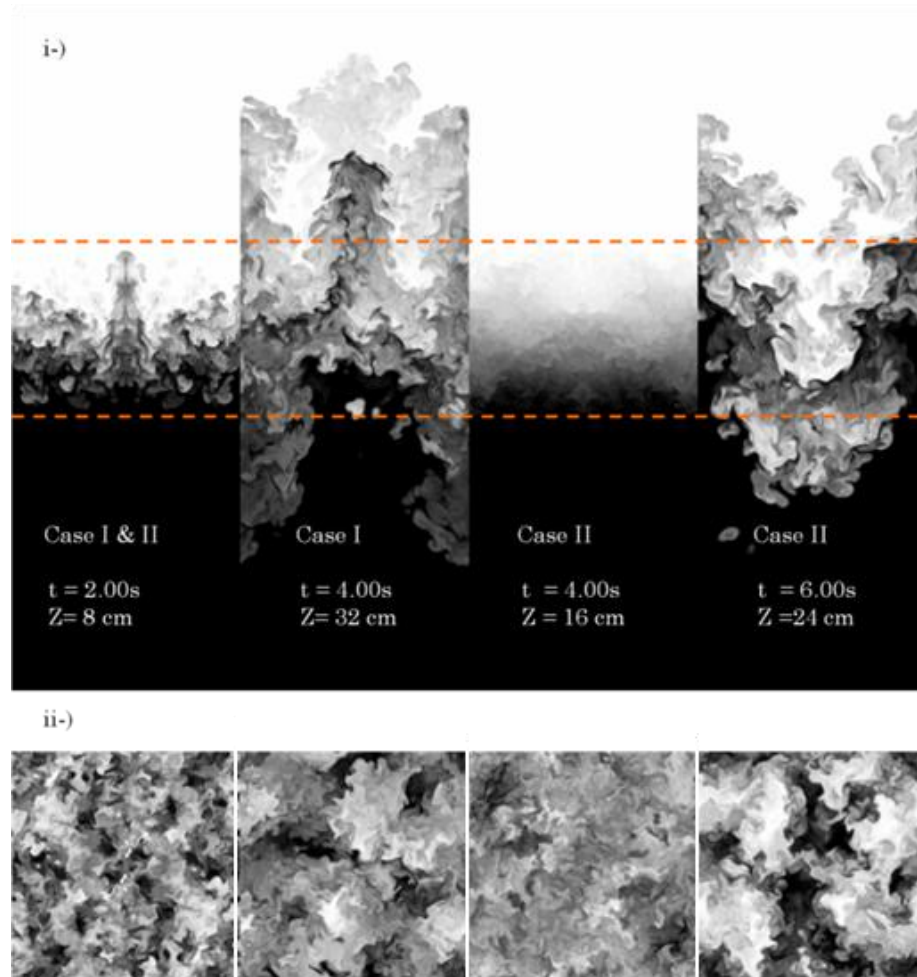
Figure 5. Density contours of the RT mixing layer (i) –XZ vertical slices taken along the center of the domain, where case I corresponds to CG_AS-0 and case II corresponds to AS-0. The vertical red dashed lines indicating the edge of the mixing layer width. (ii) corresponding – XY horizontal slices taken along the interface.

vertical slices taken along the center of the domain and corresponding (ii) horizontal slices taken along the interface at different time steps for constant gravity and the ADA profile; at constant

acceleration, the mixing layer continued to grow (*bubble competition*) and the bubbles and spikes merged to form larger structures (*bubble merger*).

The first acceleration reversal, leads to a stable stratification for the RT mixing layer (by ignoring local density variations)and conventional self-similarity mechanisms for constant acceleration RTI like *bubble merger* and *bubble competition* appear to be suspended. This decreased growth of the mixing layer (see fig. 5-i) and a decrease of total kinetic energy resulting in an increase of isotropy within the flow. The first acceleration reversal also caused a rapid change in the range of length scale observed in the flow; large structures evident at early time disintegrates due to collisions and were replaced by well-mixed small structures (see fig. 5-ii). This new scale distribution is caused by the inertia of the sudden acceleration reversal. The decomposition of the bubble and spike structures also increased the saturation of the newly formed modes.

In figure 6, bubble and spike heights are plotted as a function of the length-scale $Z(t)$, defined in eq.10. These heights are defined by the z- location of the 99% and 1% plane-averaged volume fraction values of the heavy fluid (f_h); the individual heights are measured relative to the original position of the interface ($z = 0$). $< f_h >$ is estimated as follows:

$$< f_h >= \iint f_h dxdy / L^2 \tag{13}$$

and plane averaging $<\bullet>$ of other presented quantities are done in the same manner. The vertical, dashed lines shown in figures 6-13 indicate the time-instants at which the acceleration was reversed for our ADA problem. At the end of first acceleration period ($Z = 8$), both the bubble and spike heights for the BB case remained at the highest level for bubble height (lowest level for spike height), followed by the AS--2 case whose bubble and spike heights remained between BB and AS-0 cases, and the AS-0 case which resulted in the lowest bubble and spike heights.

These three cases were all in good agreement with conventional RTI studies (see fig 6). Ramaprabhu and Andrews [21] and Banerjee and Andrews [12] reported that the simulations initialized with longer wave-lengths lead to larger growth constant values than narrow band cases. Broad band cases have larger scales at early time of the flow evolution which cause greater inertia as well as larger growth. The simulations initialized with negative spectral index values, whose mode numbers were the same as the narrow band, exhibited growth constant values that fell between those of the narrow band cases and the broad band cases. This behavior was explained due to the appearance of a higher energy proportion in its smaller mode numbers compared to narrow band cases and shorter wavelengths compared to broad band cases.
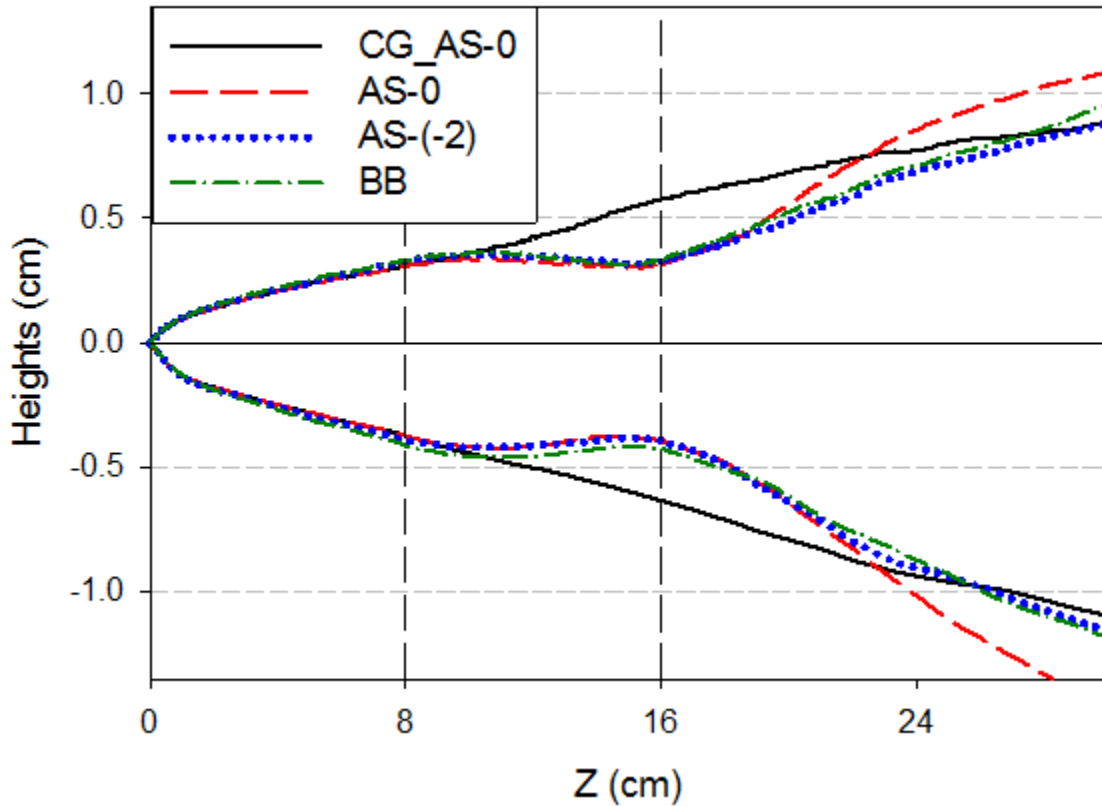
Figure 6. Evolution of the bubble (h_b) and spike heights (h_s) versus interface displacement (Z).

Corresponding α_s values for spike heights are shown in fig. 7 and reveal that during the deceleration period the growth rate of the mixing layer was IC independent. Also, for all cases, the growth speed decayed similarly. Afterward, the growth rate showed damped oscillations due to viscous effects and secondary shear. The flow, however, retained some memory of its ICs over the first acceleration and subsequent deceleration period. The mixing layer width during the re-acceleration period retained memory of the ICs and continued to play an important role in the re-growth period, which will be detailed in subsequent paragraphs.

As reported by Ramaprabhu et al. [25], after re-acceleration, the RT problem re-emerges, the mixing layer width starts to expand, molecular mixing decreases, and bubble and spike structures remerge to form larger structures. This physical process can be seen in fig. 5. Eventually, after an ICs dependent delay period (the deceleration phase), RTI self-similarity mechanisms restore themselves. On the other hand, in this study we noticed that the flow still retained the ICs information even after acceleration reversals. Moreover, the reversals not only affected the response time of the flow for new acceleration but also the behavior of the flow during this period. Since during the deceleration period the flow is mixed well, a long time is necessary to re-accelerate the fluids by re-applying positive acceleration, which leads to a delay in growth parameters (see fig.s 6 and 7), as reported by Dimonte et al. [23]. This might be attributed to the inertia of the mixed flow in the mixing layer and/or by the need for time to "un-saturate" the modes, as they are all shredded and "over-saturated" due to the first acceleration reversal.

In simulations initialized with longer wave-lengths, pure heavy and pure light fluids stayed at farther levels from the interface as the simulations grew faster during first acceleration period, which caused a longer delay time to un-saturate and to re-accelerate the flow within the

mixing layer during re-acceleration. As a consequence of this, the BB case started to re-grow after the longest delay, followed by AS-(-2) and AS-0 (see fig.6-8). BB displayed the largest structures as well as the most fully mixed volume due to its largest mixing layer width, which caused the flow to respond more gradually during re-acceleration. Thus, as seen in fig. 6, BB was not leading the flow during the re-acceleration period; AS-(-2) acted more like the BB case during late evolution of the flow, even though its response time was between those of BB and AS-0. The distinctive result from the conventional RTI studies was that at the end of simulations' run time, AS_0 led to a larger pure flow penetration and larger volume of mixing after acceleration reversals.
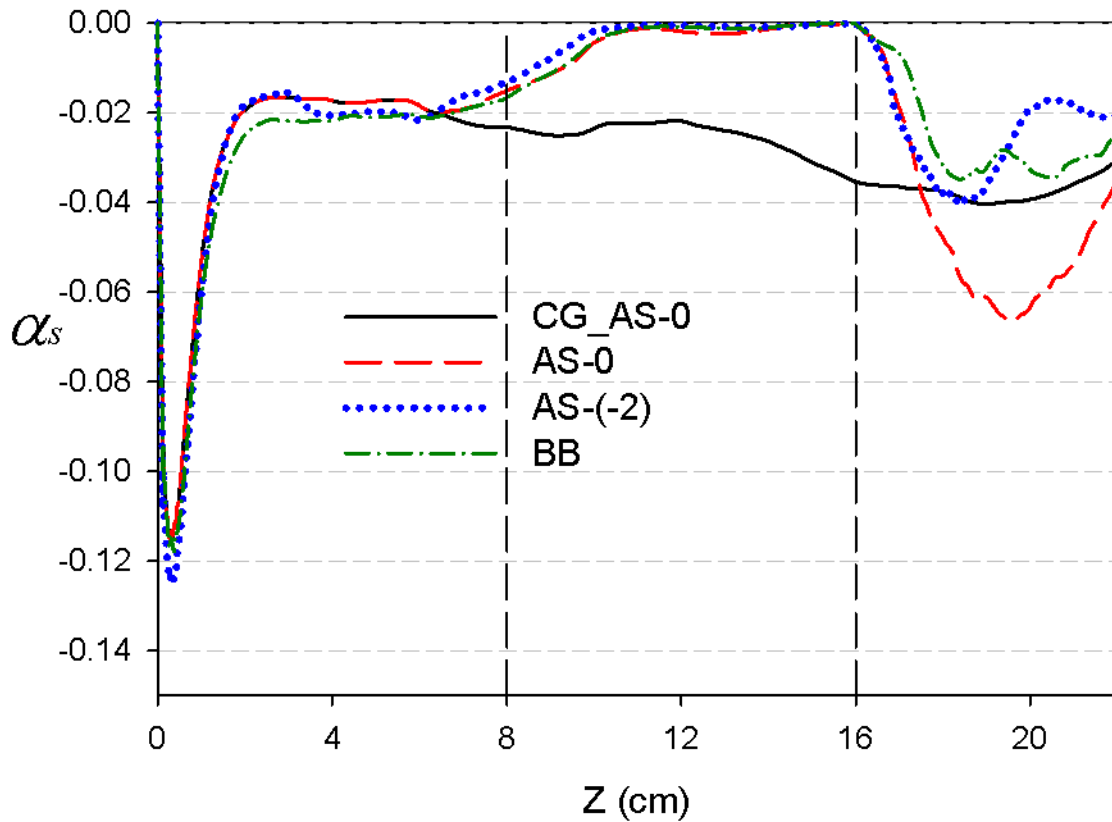
Figure 7. Evolution of the growth constant (α_s) for spikes versus interface displacement (Z).

In addition to the growth parameters, the global atomic mix parameter θ was also calculated in this study. θ values at interface is defined as:

$$\theta = \frac{\langle f_l f_h \rangle}{\langle f_l \rangle \langle f_h \rangle} \tag{14}$$

An asymptotic value of $\theta = 0.8$ was reported for the constant acceleration RTI problem [40]. The value for θ reaches 1 during deceleration, corresponding to the fully mixed flow at interface, and can be seen in fig. 8 which shows the evolution of the mixing at interface versus interface displacement (Z). During the first acceleration period, as the BB case grew faster, the amount of pure fluid passing from the interface was greater, which resulted in lower θ values (leading to less molecular mixing) for this case. During the deceleration period, all of the cases take an asymptotic value of θ equal to 1 which reiterates the observations made on mixing and over-saturation within the mixing layer that were previously made based on the density contours in a plane parallel to the direction of the mix. Upon reacceleration, the mixing layer, containing different modes and amplitudes due to variations in the ICs, went through a delay phase before it starts to re-grow. As expected, θ showed behavior similar to that observed with growth-rate parameters; since, in buoyancy driven instabilities, mass flux is the most important parameter to capture the growth of the mixing layer [43, 44] and also by definition larger mass flux causes lower θ values. For the BB case the pure fluids were farther from the interface and required a longer time to reach this boundary. As a result, the BB case started to re-grow latest and θ decreased later than other cases. Meanwhile, the AS-0 case responded to new acceleration earliest.
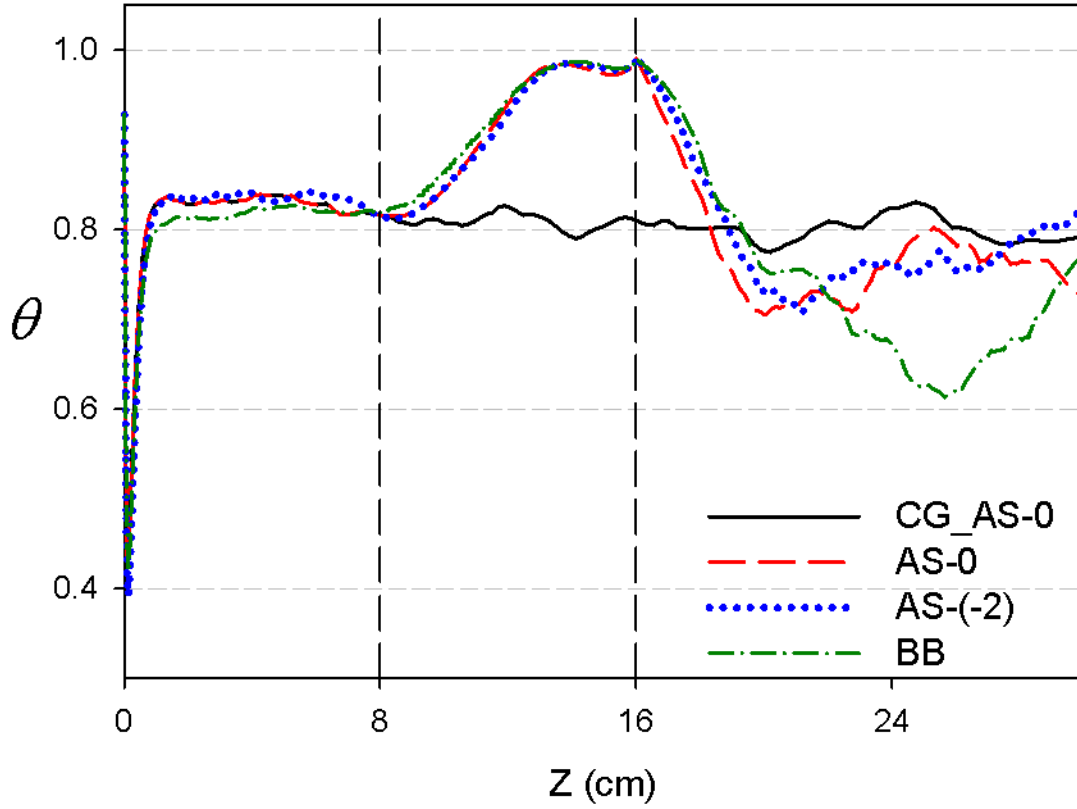
Figure 8. Evolution of the global mix parameter (θ) versus interface displacement (Z).

3.1 Second Order Moments

In the current work, second order moments were also investigated as they provide detailed information about the nature of the mixing and the concept of self-similarity in flows with acceleration reversals. A self-similar flow requires constant values for non-dimensional second order moments at the geometric center-plane, scalar (density) variance $<cc>$, non-dimensional mass flux $<u_3c>/h^{0.5}_{tot}$, and non-dimensional vertical velocity variance $<u_3u_3>/h^2_{tot}$ [40]. In this study the second order moments were averaged at the center plane (*x-y* plane at $z = 0$) that corresponded to the initial interface location for the calculations. The parameters were

non-dimensionalized by dividing the scalar by the square root of the total mix width (h_{tot} $=h_b+h_s$); the variance was divided by the h_{tot}.

From the definition of scalar variance, a low variance value corresponds to higher molecular mixing; the limiting case of fully mixed fluid has a scalar variance of zero. During the deceleration phase, where we observed a nearly fully mixed fluid within the mixing layer width, all ICs cases tend a value of zero for the scalar variance. Interestingly, the ICs effects are retained for the scalar field on reacceleration of the mixing layer. As expected, the observed effects for the scalar variance are very similar with those observed for the molecular mix parameter since both parameters are higher-order statistics of the scalar (density) field. Our next parameter is the non-dimensional $<u_3c>/h^{0.5}_{tot}$ mass flux. It has been reported in various studies that the mass flux plays a crucial role in the conversion of potential energy to kinetic energy of buoyancy driven flows [43, 44]. By reversing the acceleration (as we have stable flow) mass flux fluctuated around a value of zero (see Fig. 10) due to the secondary instabilities. The zero value indicates that there is no incoming pure fluid into the core of mixing layer width, which leads to an increase of the molecular mixing within the mixing layer.

By reaccelerating the system, we again gained positive values of the mass flux (see Fig. 10). The increase of mass-flux indicates that non-mixed fluids are again feeding the core of the mixing layer as the flow is again instable. This behavior was also related with the drop of θ seen in Fig. 8 in the previous section and also was related with the increase of the scalar variance in Fig. 9.
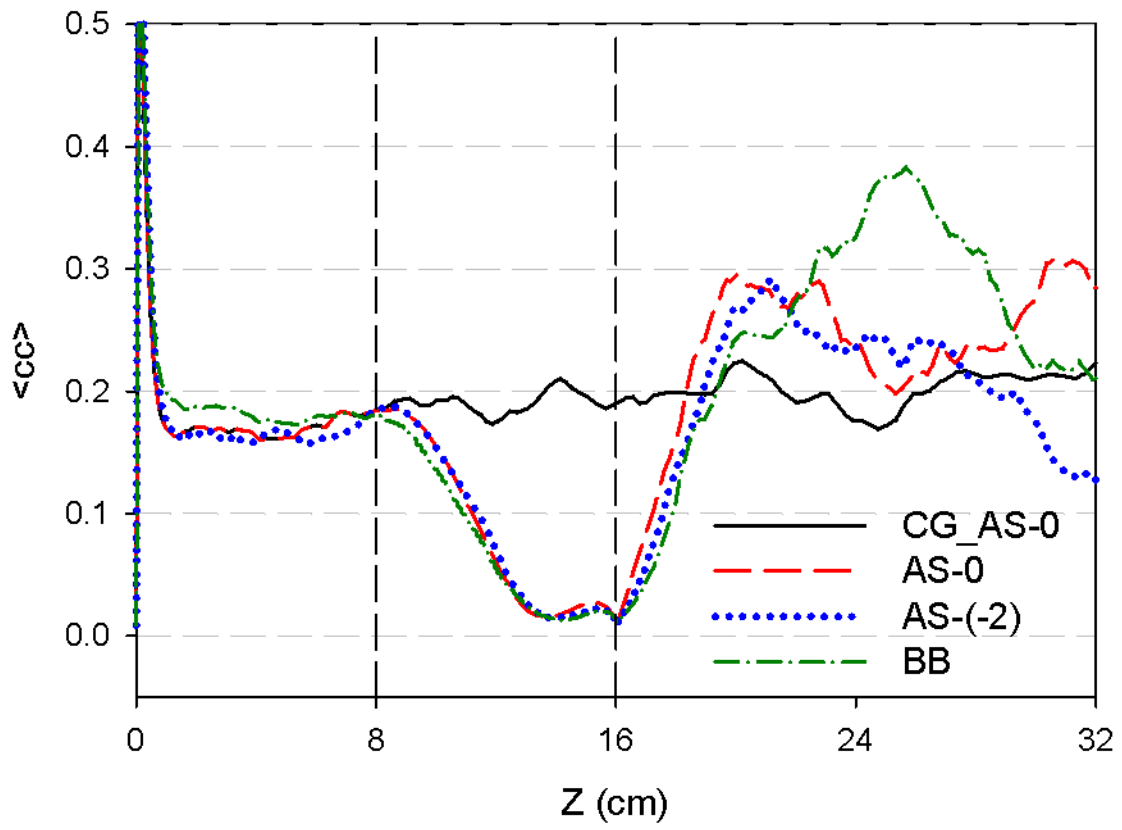
Figure 9. Evolution of scalar variance (<cc>) versus interface displacement (Z).
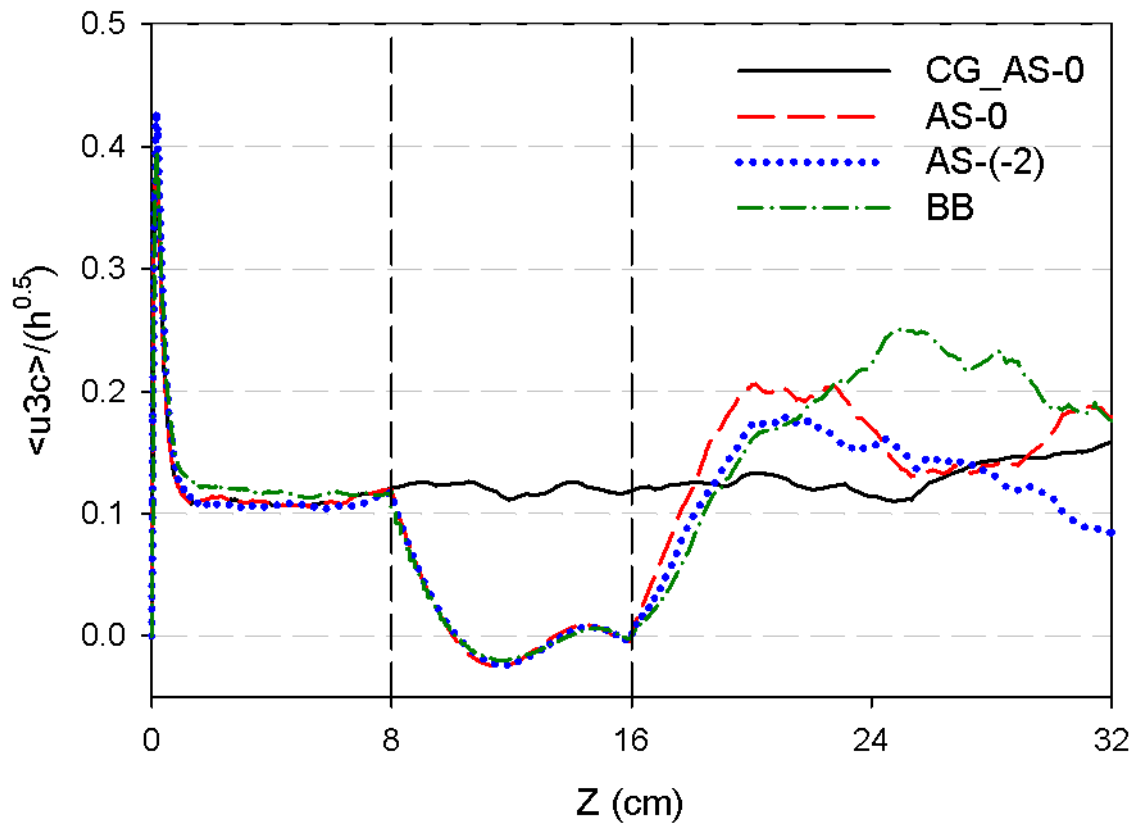
Figure 10. Evolution of non-dimensional mass flux ($<u_3c>/h_{tot}^{0.5}$) versus interface displacement (Z).

The final second order moment presented is the non-dimensional variance of the vertical component of velocity field. The mass flux values observed during the deceleration period indicates that there is no significant conversion of potential energy to kinetic energy; the residual kinetic energy in the flow undergoes decay due to viscous effects. As illustrated in figure 11, a reduction in the value of $< u_3 u_3 >$ was observed during the deceleration phase. Mass flux is also a key parameter to make a connection between second order moments of scalar and velocity variances. Thus, all three moments behaved similarly by means of ICs dependency.

During deceleration all parameters showed an increase of molecular mixing and ICs effects were not visible during this period. For reacceleration, these parameters showed some dependence on ICs and they did not reach self-similarity even at late run time's of the simulations. Our AS-(-2) case whose energy spectra had a peak over a narrow range of mode numbers reached self-similarity in a short time without much fluctuations of density field. However, by comparing its scalar and velocity variance, we noticed that its velocity field led to some fluctuation on parameters, such as mass flux and anisotropy tensor. The response time—which might be defined as: the time between the second acceleration instant to the point where the parameter first touches its asymptotic value observed—was shortest for our narrow-band case (AS-0), which had shorter wavelengths compared to other cases. The BB case, which was composed by smaller and more gradual acts compared to other cases, presented a delayed response. AS-(-2) case's response time was observed to be between these two cases. By means of self-similarity during the first acceleration period, we have reached to the self-similarity at interface in terms of second order moments. However, acceleration reversal, which leads to suspension of RTI self-similar mechanisms, also broke the self-similarity. Thus self-similarity was not able to be reassumed during the second-acceleration period in our simulation run time.
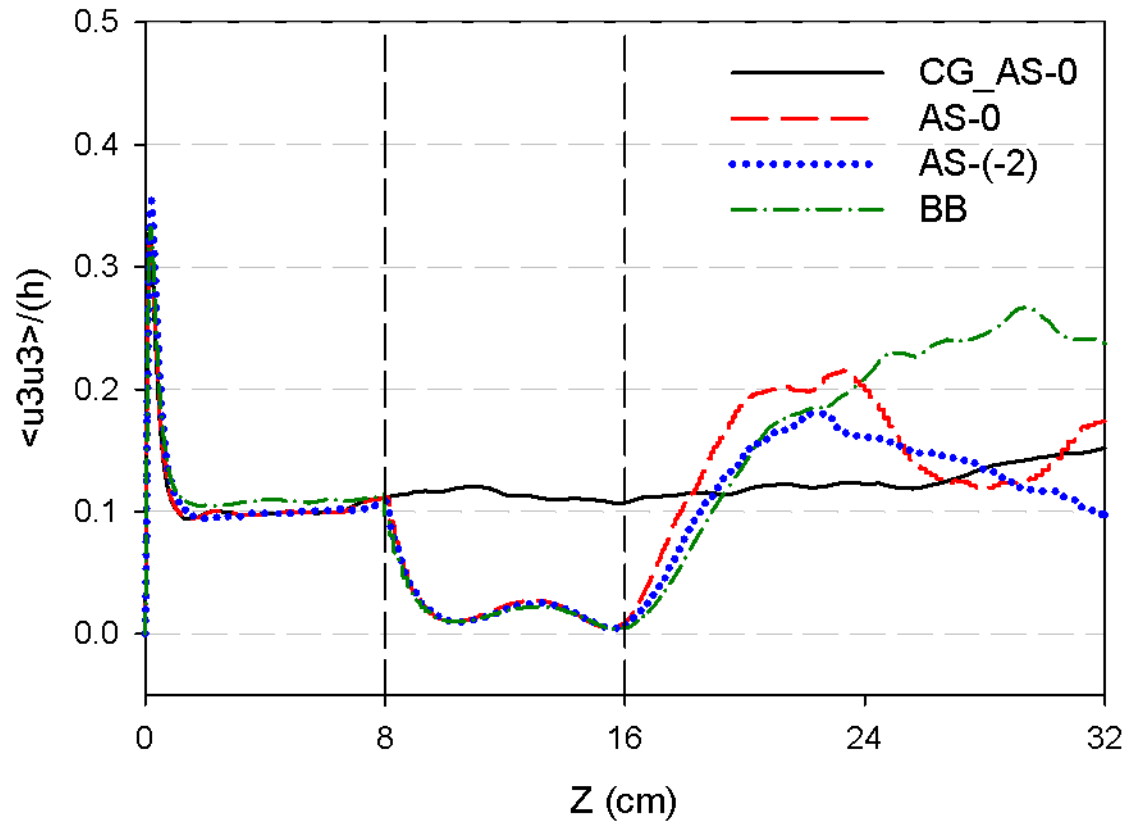
Figure 11. Evolution of non-dimensional vertical velocity variance ($<u_3u_3>/h_{tot}$) versus interface displacement (Z).

3.2   Anisotropy Tensors

The anisotropy tensor provides information about the rate of total kinetic energy in the corresponding direction, which is always bounded between -1/3 and +2/3. -1/3 implies no energy in the measured component whereas 2/3 implies all energy is in that component. As a result, B_{33} indicates the amount of total energy in the vertical component while B_{11} and B_{22} refer to the horizontal components and are calculated as:

$$B_{ij} = \frac{<u_i u_j>}{<u_k u_k>} - \frac{1}{3}\delta_{ij} \tag{15}$$

Isotropic flow requires the components of anisotropic tensor components to be equal: $B_{11} = B_{22} = B_{33} = 0$, so from eq. 15 all components should be zero. RTI requires horizontally isotropic flow where $B_{11}=B_{22}$ and vertically anisotropic flow. The asymptotic value of B_{33} was reported as ~0.30 in Ristorcelli and Clark's study [40] which is ~%66 of the total energy. The rest of the total energy lies in horizontal components of the anisotropy tensor and each of them approaches a value of -0.15. Figure 12, shows all of the components of the anisotropy tensor for our comparison case, CG_AS-0, under constant acceleration. During the deceleration period, as the total kinetic energy decayed, the isotropy within the flow increased. Here the anisotropy tensor presented a difference from the other presented parameters, showing ICs dependence even during the deceleration period indicating that the flow does not lose the memory of the initial conditions even after acceleration reversal. We attribute this to the fact that horizontal movements and their statistics are as important as the vertical ones in preserving ICs information, especially during the deceleration period. This ICs dependency is also a valuable proof for the idea that ICs' effects will appear somehow after second reversal.

Fig. 13 reveals similar behaviors between anisotropy tensor and the parameters already presented. The broad-band case acted more gradual even during the deceleration period and it

responded to re-acceleration with a longer delay. In terms of self-similarity, even anisotropy tensor did not reach self-similarity at the end of our simulation time after acceleration reversals. Our narrow band case with spectral index value -2 (AS-(-2)) stayed at lower values, indicating more isotropy within the flow. This can be explained by its non-flat spectra (unstable distribution of energy between mode numbers), which caused larger horizontal movements than other cases and decreased the anisotropy of the flow.
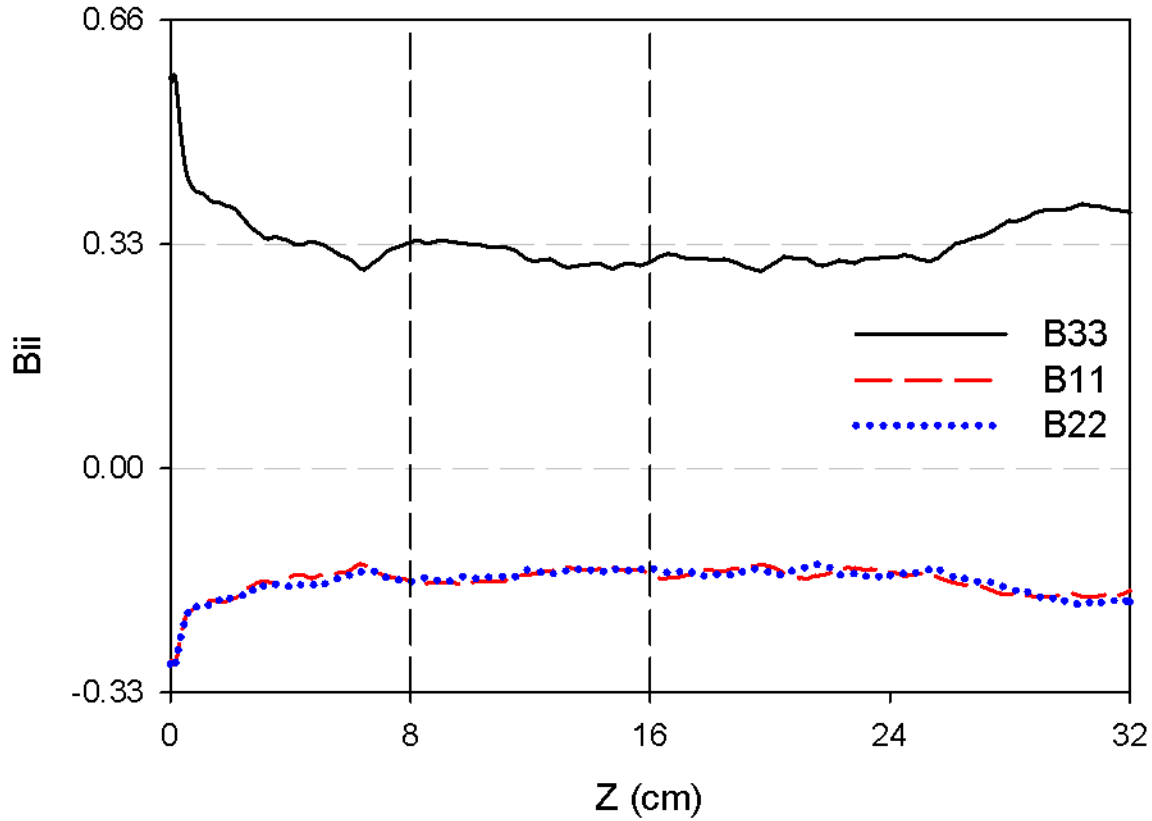
Figure 12. Evolution of Anisotropy Tensors B_{33}, B_{11} and B_{22} for constant acceleration case versus interface displacement (Z).
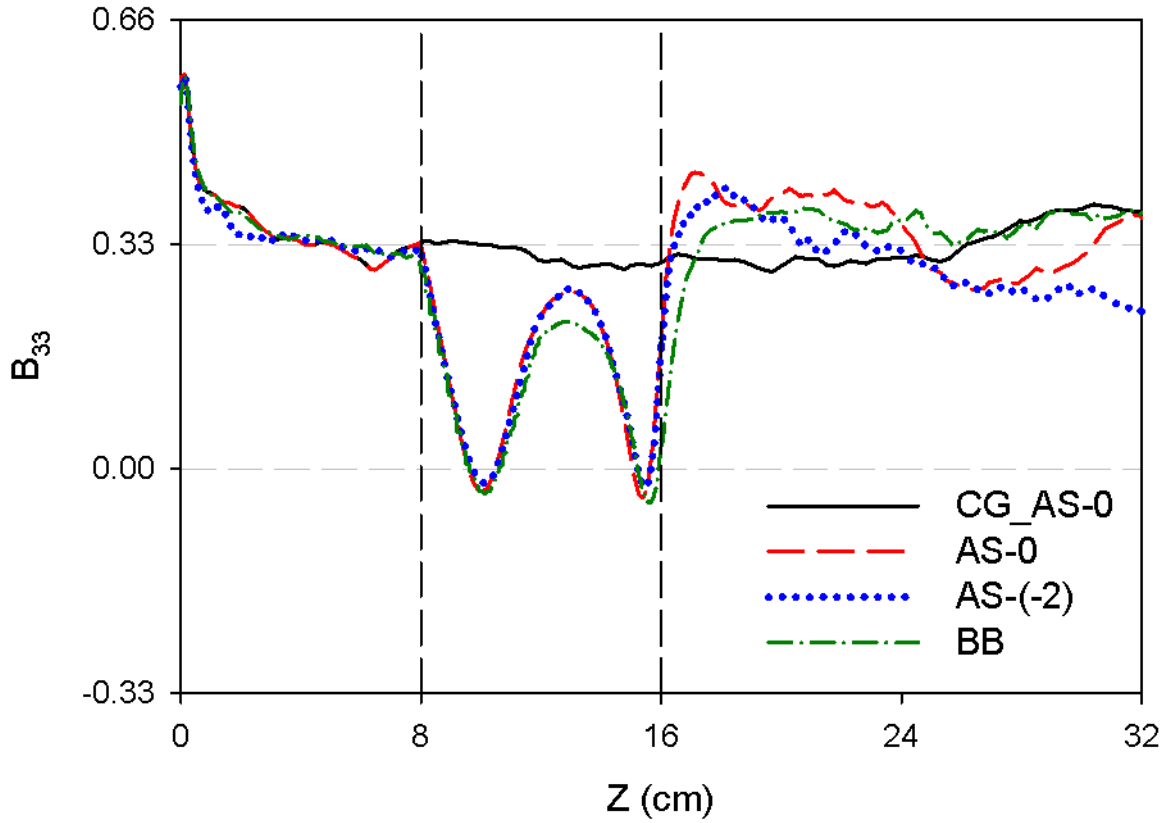
Figure 13. Evolution of Anisotropy Tensor B_{33} versus interface displacement (Z).

3.3 Spatial Profiles

Spatial profiles of the second order moments provide information about the structure of the flow. Ristorcelli and Clark [40] report spatial profiles of the parameters reported in §3.2 and for their RTI simulations under constant acceleration history. The reported simulations were Boussinesq (A_t=0.01) resulting in highly symmetric profiles on both sides of the geometric centerline. However, in our study, the Boussinesq assumption is no longer valid at our moderate Atwood ($A_t = 0.5$) numbers. Non-Boussinesq effects are observed to significantly affect the spatial profiles, and the symmetry at the interface is lost..

We start the discussion by reporting spatial profiles of parameters for our base case (AS-0) for both CG and ADA profiles for the case of the annular spectrum (AS-0); the objective is to understand the spatial evolution of the profiles for CG and ADA histories without the additional complexity of IC effects (see fig.s 14, 15 and 16). The $-x$ axes of the figures, which display the profiles, correspond to the non-dimensional height of the domain. For non-dimensionalizing in figures 14, 15 and 16 the domain height $-z$ was divided with the value of $(h_b+h_s)/2$ for CG_AS-0 case at Z=32; and for figures 17, 18, 19 and 20 the domain height $-z$ was divided with the value of $(h_b+h_s)/2$ for AS-0 at corresponding Z values. The boundary condition was no-flux in the $-z$ direction; therefore, horizontal and vertical velocity variances and scalar variance values were zero at the edges of the domain (see fig.s 14 and 16) as the vertical component of the anisotropy tensors was negative 0.33, indicating no energy in that component (see fig. 15). For Boussinesq case spatial profiles of the second order, moments correspond fairly well with a Gaussian distribution [40], whereas non-Boussinesq effects led to a flat peak of spatial profiles as seen in fig. 14. The flat region might be called a "mixing core", which starts and ends where the mean concentration is 40% and 60% of the field. Additionally, there is an edge region, defined as where the mean concentrations are 5% and 95% of the far field [40], the transition region, between the edge region and mixing core, and which is defined as where the mean concentration is between 5% to 40%, and 60% to 95% of the field, and the flat region of the velocity variances, (see fig 14) called the mixing core.
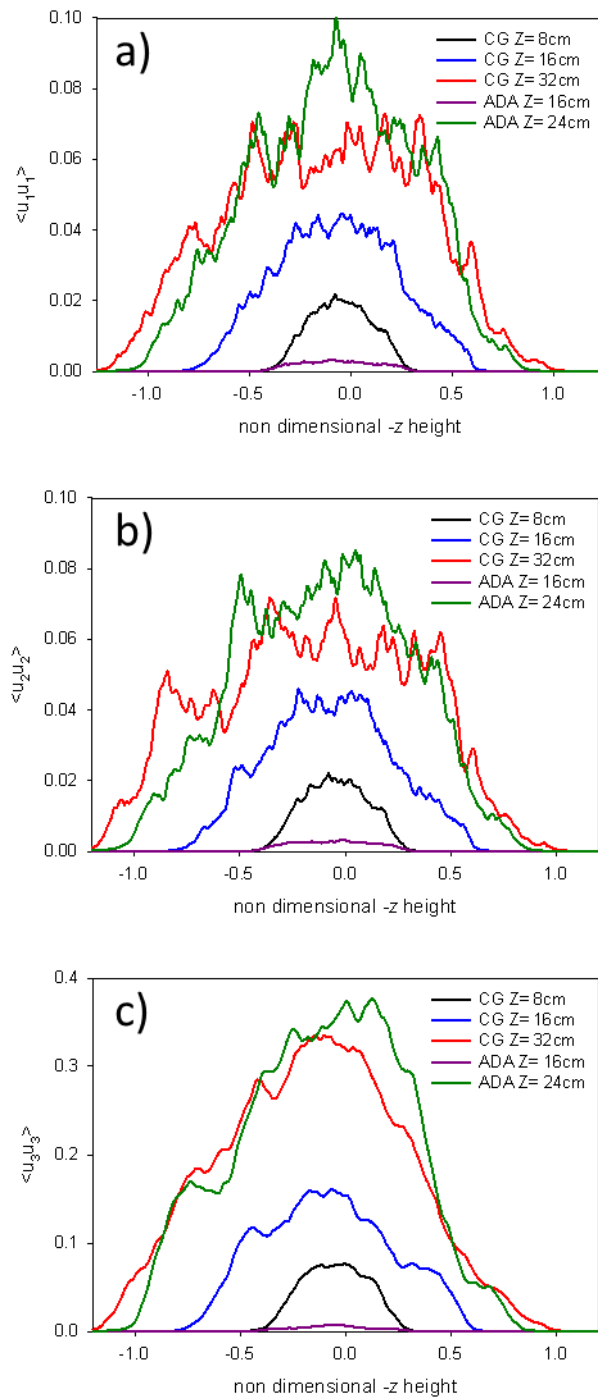
Figure 14. Spatial profiles of a) $\langle u_1 u_1 \rangle$, b) $\langle u_2 u_2 \rangle$ and c) $\langle u_3 u_3 \rangle$ for both CG_AS-0 and AS-0 at different Z values.
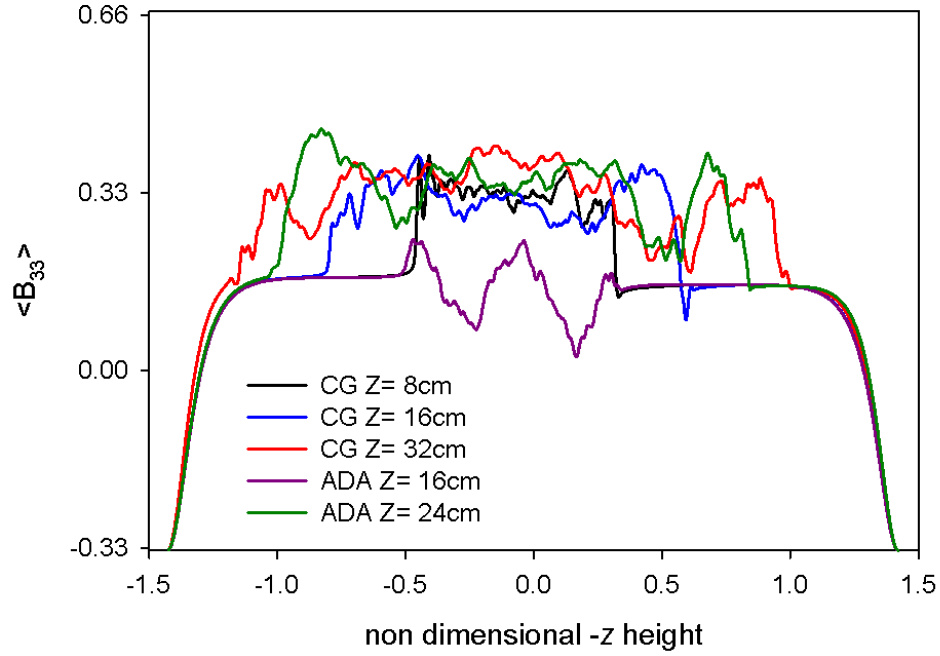
Figure 15. Spatial profiles of B_{33} for both CG_AS-0 and AS-0 at different Z values.
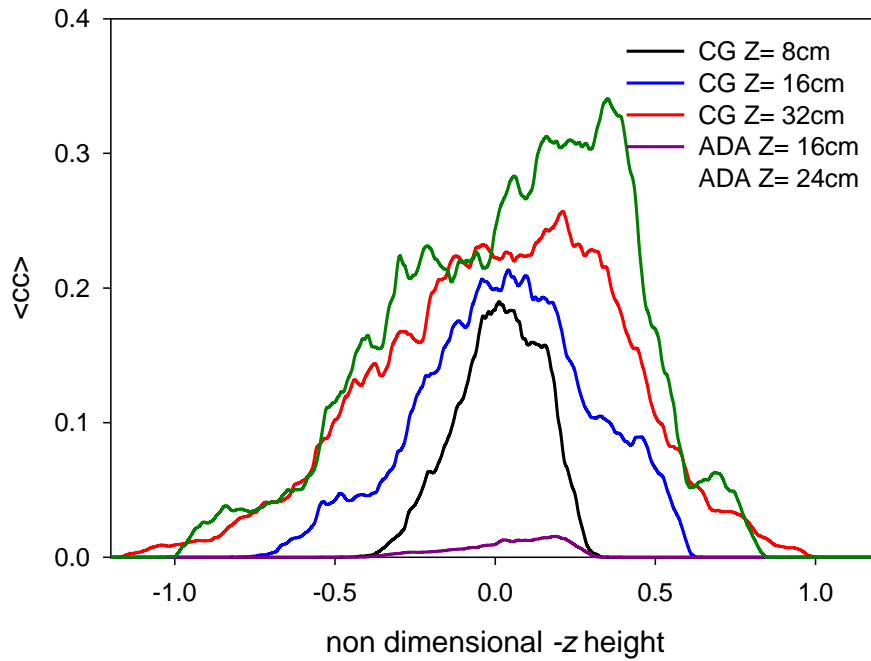
Figure 16. Spatial profiles of <cc> for both CG_AS-0 and AS-0 at different Z values.

Besides the flat peak, there is an additional significant difference between Boussinesq and non-Boussinesq cases having symmetry at interface. As it was seen in Figure 6, heavier fluid is penetrating into the lighter fluid faster than the lighter fluid's penetration. This disparity is also clearly observable in the spatial profiles (see fig.s. 14, 15, and 16), as the edge region of mixing layer starts at different levels for heavier and lighter fluids' sides, such as in fig. 16 in which the edge region of the red line, corresponding to the spatial profile of the scalar variance for CG_AS-0 case at Z=32 cm, starts from non-dimensional -z value of *-1.2* but ends at value of *1*. The asymmetric profiles in fig. 16 might be also attributed to the difference between light and heavy fluids' involvement of material mixing like that in Livescu and Ristorcelli [45], who found that light fluid mixes faster than heavier. Since the molecular mixing was increasing during the deceleration period, the asymmetry increased at the end of deceleration period. By looking at anisotropy tensor plot (see fig. 15), it is seen that except at the edges of the domain, the flow is not isotropic even at pure fluids' levels where the vertical component of the anisotropy tensor is around 0.1 beyond the mixing layer width. Opposite to the velocity and scalar variances' spatial profiles, the spatial profile of the anisotropy tensor has a step function profile and immediately increases to values around 0.3, the asymptotic value of B33 for RTI flow, within the mixing layer width.

Spatial profiles are also presented in figures 17, 18, 19 and 20 to study ICs effects. The edge region and mixing core are important to determine the differences between ICs; whereas, the transition region of the spatial profiles are similar for all cases. At the end of first acceleration period (Z=8cm), the BB case had the longest height of non-zero velocity variance, having the fastest mixing layer growth, and was followed by AS-(-2) and then AS-0 (see fig. 18). These were consistent with mixing layer width calculations (see fig. 6). Similar to the time evolution of

second order moments at the interface, second order moments' spatial profiles also did not give any detailed information by means of ICs' role during the deceleration period. At the end of this period (Z=16cm), velocity and scalar variances tended to reach the value of zero as the flow is conventionally stable.
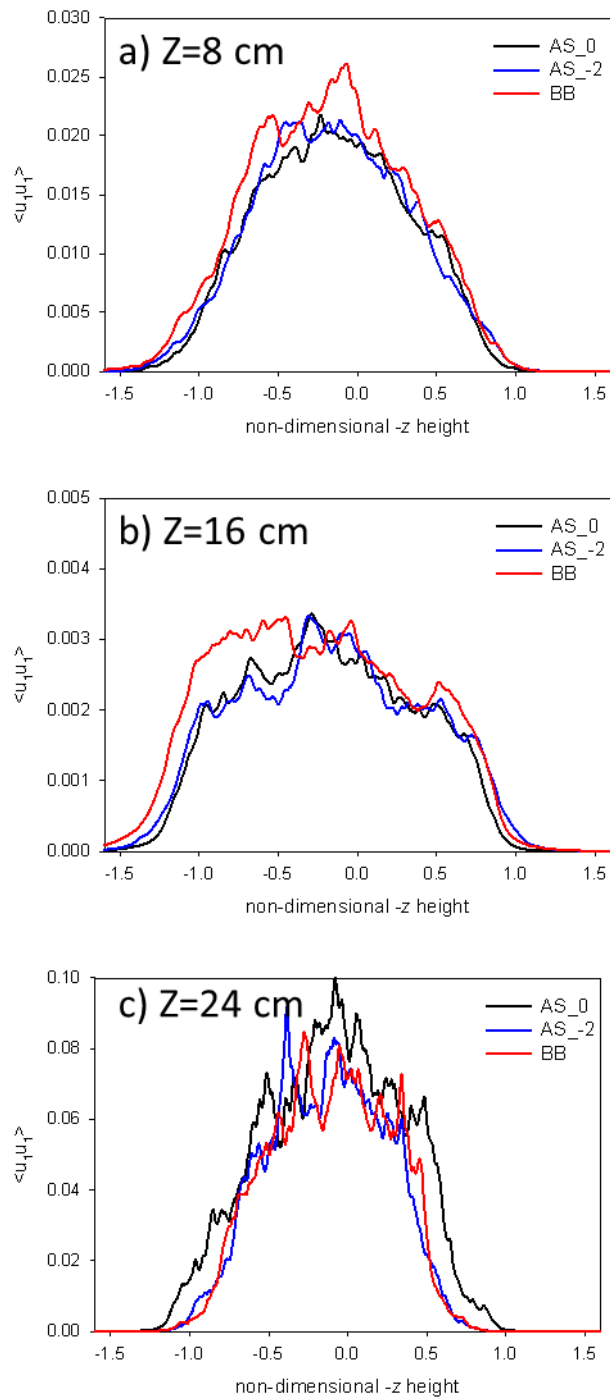
Figure 17. Spatial profiles of $\langle u_1 u_1 \rangle$ at a) Z= 8 cm b) Z =16 cm and c) Z=24 cm for all ICs.
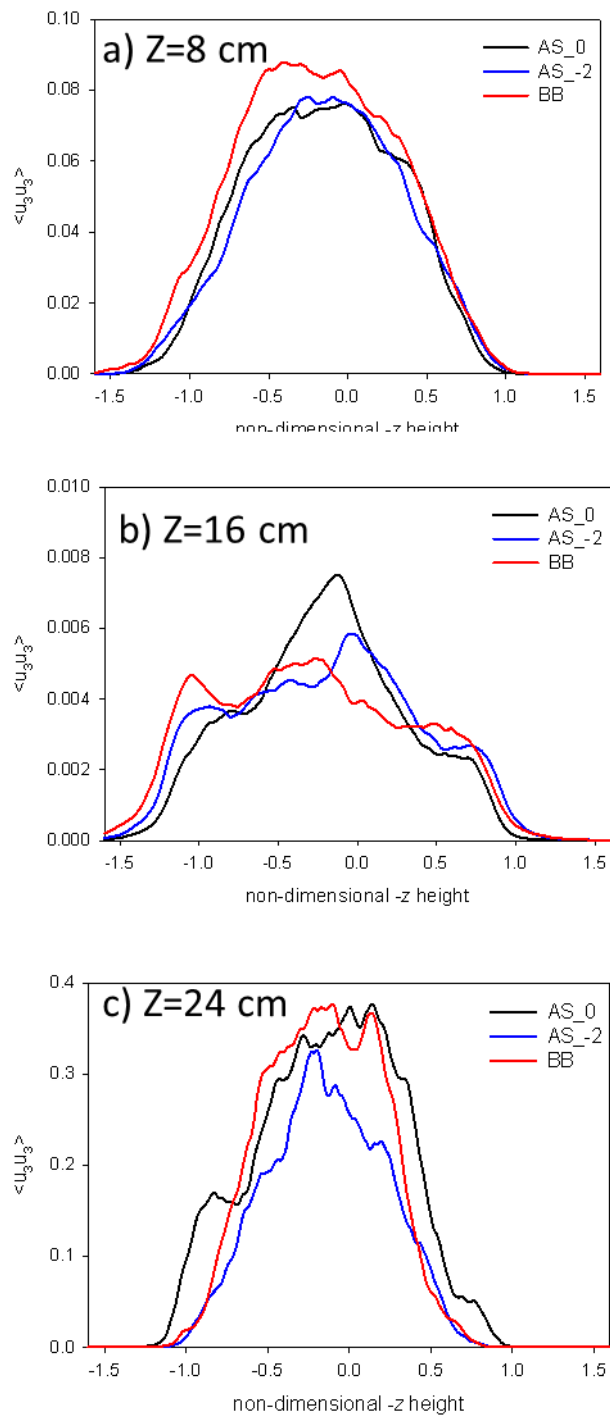
Figure 18. Spatial profiles of $\langle u_3 u_3 \rangle$ at a) Z= 8 cm b) Z =16 cm and c) Z=24 cm for all ICs.
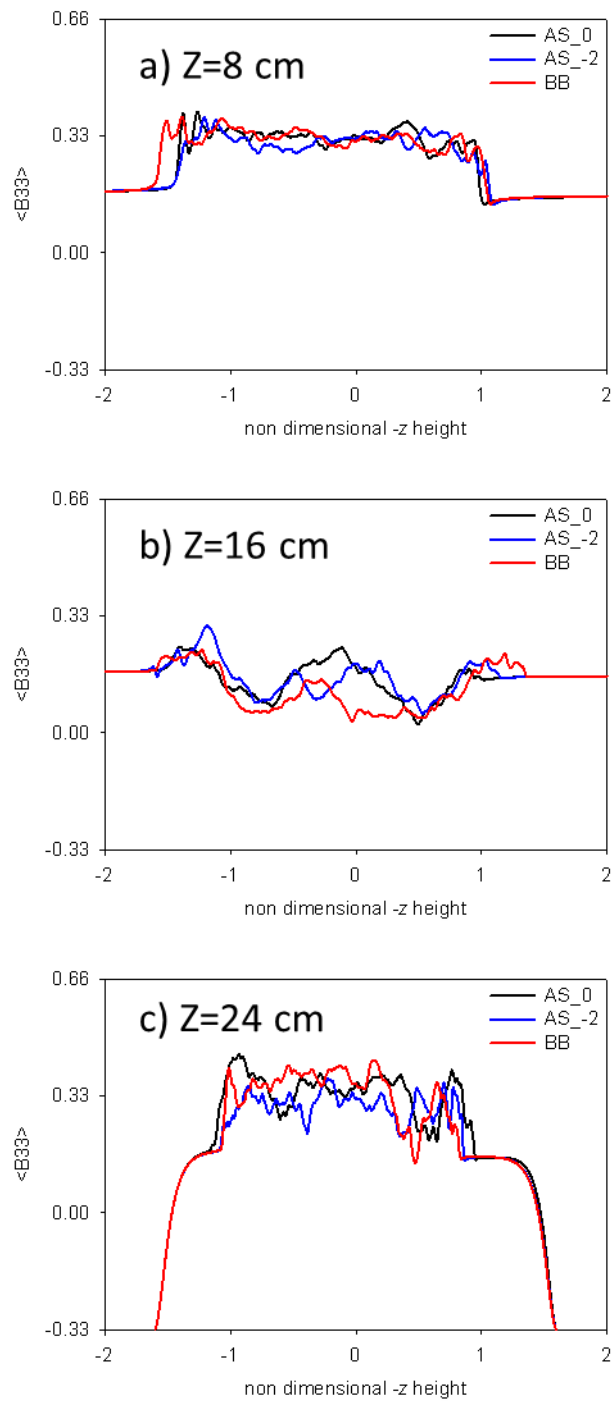
Figure 19. Spatial profiles of B_{33} at a) Z= 8 cm b) Z =16 cm and c) Z=24 cm for all ICs.
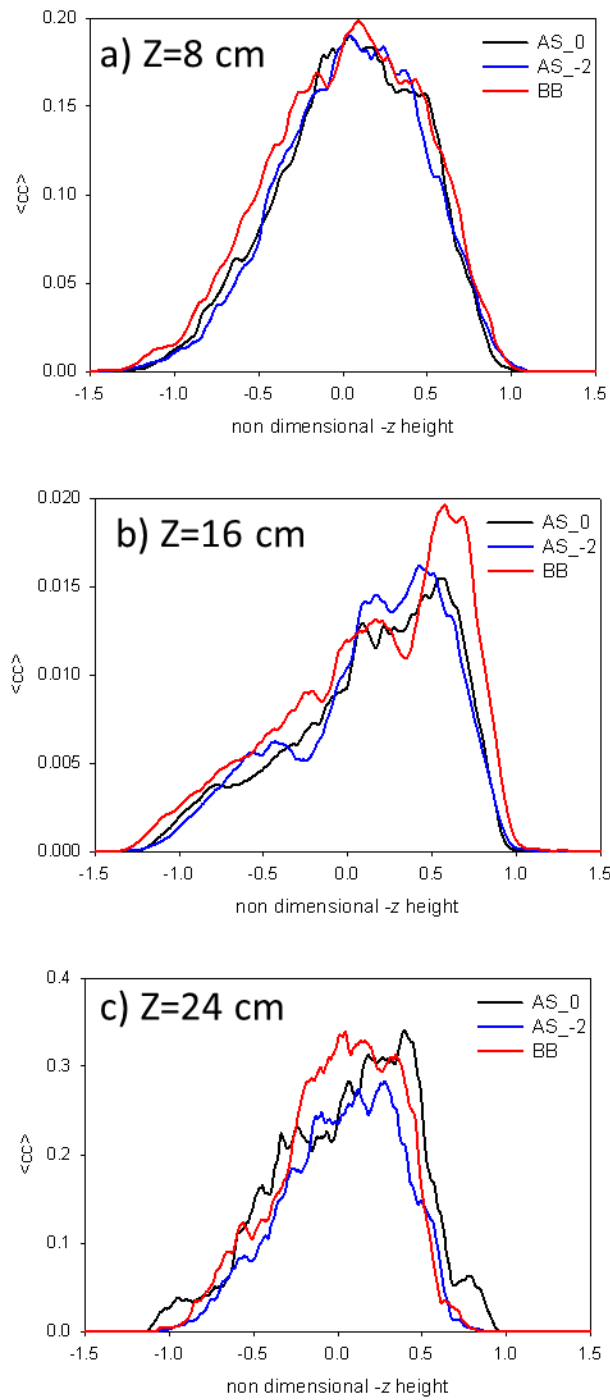
Figure 20 Spatial profiles of <cc> at a) Z= 8 cm b) Z =16 cm and c) Z=24 cm for all ICs.

The asymmetric behavior of the scalar variance increased. Due to the lighter fluid and the fact that its involvement in molecular mixing is greater than the heavier fluid's involvement, the scalar variance had lower values at lighter fluid's side (see fig. 20). On the other hand, the anisotropy tensor did not settle (see fig. 19) and continued fluctuating with large amplitudes even after the declaration period. However, the fluctuations seen in these spatial profiles were not enough to clearly distinguish the ICs effects.

After the second acceleration reversal where the interface displacement was 24cm, spatial profiles of velocities' and scalar variances showed some ICs dependency; meanwhile, the anisotropy tensor's spatial profile did not give any information about the ICs effects. The vertical component of the anisotropy tensor was arbitrarily fluctuating within the mixing layer for all ICs around its asymptotic value of 0.3. The edge regions' of the BB case's velocity and scalar variances did not start from lower values than other cases anymore, as the velocity had been increasing more slowly after acceleration reversals (see fig.s 17, 18, 19, and 20). Thus, the AS-0 case had a wider spectra of spatial profiles, followed by the AS-(-2) and BB cases. Finally, the magnitude of the vertical velocity variance at the mixing core did not provide any information about the ICs' effects since they are not total velocity and are only fluctuations of the velocity.

4. CONCLUSION

The RTI problem was investigated in order to understand the late time evolution due to turbulence with different ICs under the ADA profile, by a massively parallel three–dimensional, variable-density, in-compressible flow solver (MOBILE) that uses the ILES technique. Narrow-band with SI=0, narrow-band with different spectral shape (SI=-2), and broad-band cases were compared to identify ICs effects on self-similar evolution of RTI under ADA.

During the first acceleration period, results were consistent with literature investigating ICs effects on classical RTI (no acceleration reversal) [12, 13, 18]; the cases with longer wavelengths grew faster than the narrow band cases. The SI value was -2, falling between the narrow and broad band cases, had larger energy proportion in its smaller wave numbers. After the first acceleration reversal (A→D), growth and mixing parameters reached their asymptotic values after only a short time, with oscillations due to viscous effects observed in all cases. The growth of the mixing layer stopped after a while and the global atomic mix parameter approached a value of 1, indicating "fully mixed" flow at the interface. From this A-D segment, it is expected that the molecular mixing volume might be changed by altering the IC, and as from the results presented, it is seen that the mixing layer width stays at different levels for different ICs.

After the second acceleration reversal (D→A), the RTI problem reemerges and the atomic mix parameter by mode dependently where the mixing layer started to grow again. Bubble and spike structures merged to form larger structures, which was one of the self-similarity mechanisms for RTI. As was explained in the results section, the response time to the acceleration reversals were directly affected by ICs. For this reason, the narrowest band case (AS-0) had shorter delays than the AS-(-2) and BB cases. The most remarkable result occurred

during the re-acceleration period. In addition to exhibiting a delayed response, the flow in BB acted significantly more gradual and did not dominate the growth during re-acceleration. Additionally, it was observed that during the re-acceleration period the mixing layer width grew faster than during the first acceleration period; although, the comparison rates were directly affected by initial conditions. Finally, we noticed that at the end of our simulations' run time, even alpha values tended to reach their asymptotic values for all cases, and theta still continued to fluctuate around its asymptotic value 0.8.

Spatial profiles of the second order moments ($<u_iu_i>$ and $<cc>$) and the vertical component of the anisotropy tensor (B33) were also investigated to improve the understanding of the flow's structure. Spatial profiles of the second order moments reinforced the role of non-Boussinesq effects and revealed the asymmetric structure of the flow. The asymmetry explains the difference between light and heavy fluids' involvement of material mixing reported by Livescu and Ristorcelli [45], and reinforces the different values of the bubbles' and spikes' heights. It is shown that the starting and ending points of the edge regions of the spatial profiles are directly related to the cases' h_b and h_s. On the other hand, the transition region and mixing core of the spatial profiles did not reveal any information about the ICs effects.

The results showed that ICs continued to strongly affect the RT mixing, even after reversals in acceleration histories. The study serves as a motivation for further detailed investigations of ICs effects on RTI under variable acceleration. After acceleration reversals, the ICs' behavior dramatically changed compared to the conventional RTI studies, which promises a great opportunity to understand the physics ongoing in applications such as ICF capsules where RTI is driven by time-varying acceleration, albeit with the consideration that the results presented need to be further validated using larger simulations/direct numerical simulations and

with a wider range of parameters such as higher order moments, RTI energetics, and spatial parameters.

APENDIX A

The FORTRAN script of Annular Spectra (AS) ICs' numeric:

```
c234567------------------------------------------------------------
-------
c##################################################################
#####
c
c##################################################################
#####

      program amplitude
      implicit real*8(a-h,o-z)

c##################################################################
#####
c Choose max and min wave number for ICs. A 128x128 calculation should
not
c have kmax > 32.
c##################################################################
#####

      parameter (kmin=16,kmax=32)
      parameter (nx=128, ny=128)
c      parameter (nx=256, ny=256)
      dimension h(nx,ny)

c##################################################################
#####
c Parameter trms is the target rms for the initial perturbations.
Refer to
c  Dimonte et al (POF - 2004) for definition. The parameter SI is the
c  spectral index. Please refer to Banerjee & Andrews (IJHMT, 2009)
c##################################################################
#####

      parameter (trms=0.000315)
      parameter (SI=0)

c##################################################################
#####
c Seed for random number generator
c##################################################################
#####

      idum=-1
      pi=4.0*atan(1.0)
      dx=2.0*pi/float(nx)
      dy=2.0*pi/float(ny)
```

```
c######################################################################
#####
c Initialize the perturbation
c######################################################################
#####

      do 100 j=1,ny
      do 100 i=1,nx
     h(i,j)=0.0
100       continue
c Outer loop where we add each wavenumber perturbation
          do 1010 iwave=1,5000
     if(mod(iwave,100).eq.0) write(*,*) ' Done',iwave,' waves'
c Randomly select the wavenumber, then the amplitude of the wave
          fk=float(kmin)+int(float(kmax-kmin)*ranmja(idum))
           amp=2.0*(0.5-ranmja(idum))*(fk)**(SI)
c Now randomly select the angle of the wave trajectory in x-y space
        angle=ranmja(idum)*2.0*pi
c       angle=0.0
c Assign x-y wavenumbers
        fkx = int(fk*cos(angle))
        fky = int(fk*sin(angle))

c Randomly select the phase and its associated x-y phase displacements
c        pxy=2.0*pi*ranmja(idum)
        pxy=0.0
     px=pxy*fkx/fk
     py=pxy*fky/fk


c######################################################################
#####
c Loop over domain and assign the wave
c######################################################################
#####

      do 500 j=1,ny
        y=dy*float(j)-dy/2.0
         do 500 i=1,nx
          x=dx*float(i)-dx/2.0
          h(i,j)=h(i,j)+amp*(cos(fkx*x+px)*cos(fky*y+py)-
     &                   sin(fkx*x+px)*sin(fky*y+py))
500         continue
1010    continue

c######################################################################
#####
c Compute RMS of the perturbation
c######################################################################
#####

      do 1200 j=1,ny
      do 1200 i=1,nx
```

```
            rms=rms+h(i,j)**2
1200         continue
      rms=sqrt(rms/float(nx*ny))

c####################################################################
#####
c Adjust h values to target rms
c####################################################################
#####

         do 5 j=1,ny
          do 5 i=1,nx
            h(i,j)=h(i,j)*trms/rms
5          continue

c####################################################################
#####
c Compute new RMS of the perturbation
c####################################################################
#####

      do 1500 j=1,ny
      do 1500 i=1,nx
        nrms=nrms+h(i,j)**2
1500         continue
      nrms=sqrt(nrms/float(nx*ny))

c####################################################################
#####
c  Write to data file - name date file according to your
specifications
c  Example: A 128x128 data file with modes 4-16 (SI=0) can be named
as:
c    "M128k4-16SI0.dat"
c####################################################################
#####

            write(*,*) ' rms=',nrms,' rms^2=',nrms*nrms
      write(*,*) ' About to write perturbation file'
      open(9,file='M128k4-16SI0.dat')
      do 2000 j=1,ny
      do 2000 i=1,nx
      write(9,*) h(i,j)
2000         continue
      close (9)
      stop
      end

c####################################################################
#####
      function ranmja(idum)
c
```

```fortran
c Function:    A Random generator from Numerical Recipies
c Author:      M.J. Andrews
c Date:        Sept 1991
c
      implicit real*4 (m)
      parameter (mbig=4000000.0, mseed=1618033.0, mz=0.0, fac=1./mbig)
      dimension ma(55)
c NEXT line added by MJA because my complier does not
c automatically save values between function calls!
      save inext, inextp, ma
      data iff/0/
      if(idum.lt.0 .or. iff.eq.0) then
        iff=1
        mj=mseed-iabs(idum)
        mj=mod(int(mj),int(mbig))
        ma(55)=mj
        mk=1
        do 11 i=1,54
          ii=mod(21*i,55)
          ma(ii)=mk
          mk=mj-mk
          if(mk.lt.mz) mk=mk+mbig
          mj=ma(ii)
11      continue
        do 13 k=1,4
          do 12 i=1,55
            ma(i)=ma(i)-ma(1+mod(i+30,55))
            if(ma(i).lt.mz) ma(i)=ma(i)+mbig
12        continue
13      continue
        inext=0
        inextp=31
        idum=1
      endif
      inext=inext+1
      if(inext.eq.56) inext=1
      inextp=inextp+1
      if(inextp.eq.56) inextp=1
      mj=ma(inext)-ma(inextp)
      if(mj.lt.mz) mj=mj+mbig
      ma(inext)=mj
      ranmja=mj*fac
      return
      end
```

APENDIX B

The MOBILE is calculating density and velocity fields as well as pressure term. The rest of calculations (presented parameters) were explicitly calculated by the following FORTRAN script. The mathematical operators are written in the code and can be found in Lawrie, A.G.W.'s Doctorate Dissertation [27].

Apendix B-i

input_postp_interface.dat :

```
begin();
iz:=variable(matrix[1]);
iz:=assign(0);
control:=variable(matrix[1]);
control:=assign(0);
rho:=variable(matrix[tnz]);
rho:=assign(0);
#f_lf_h:=variable(matrix[tnz]);
#f_lf_h:=assign(0);
theta_1:=variable(matrix[tnx,tny]);
theta_1:=assign(0);
rho_1:=variable(matrix[1]);
rho_1:=assign(0);
theta:=variable(matrix[1]);
theta:=assign(0);
h:=variable(matrix[tnz]);
h:=assign(0);


uvel:=variable(matrix[tnx,tny]);
uvel:=assign(0);
vvel:=variable(matrix[tnx,tny]);
vvel:=assign(0);
wvel:=variable(matrix[tnx,tny]);
wvel:=assign(0);
scal:=variable(matrix[tnx,tny]);
scal:=assign(0);

###width calculations
#

label('zz1loop');
rho[iz]:=meanvalue(scal0[:,:,iz]);
#f_lf_h[iz]:=multiply(scal0[:,:,iz],scal1[:,:,iz]);
iz:=add(iz,1);
if(iz,GE,tnz,'print','zz1loop');
```

```
#
label('print');
h:=add(rho,-1);
h:=multiply(h,rho);
h:=multiply(h,-6);
h:=divide(h,tnx);
h[tnz/2]:=meanvalue(h);
h[tnz/2]:=multiply(h[tnz/2],tnz);
rho_1:=meanvalue(scal1[:,:,tnz/2]);
theta_1:=multiply(scal0[:,:,tnz/2],scal1[:,:,tnz/2]);
theta:=meanvalue(theta_1);
theta:=divide(theta,rho[tnz/2]);
theta:=divide(theta,rho_1);
'theta':=print(theta,TIMEFORMAT);
'rho':=print(rho,TIMEFORMAT);
#'f_lf_h':=print(f_lf_h,TIMEFORMAT);
'h_Z':=print(h[tnz/2],TIMEFORMAT);
iz:=assign(0);

#######

label('cont');
#out_put_files


cc:=variable(matrix[1]);
cc:=assign(0);
c^3:=variable(matrix[1]);
c^3:=assign(0);
c^4:=variable(matrix[1]);
c^4:=assign(0);
u_3c:=variable(matrix[1]);
u_3c:=assign(0);
u_3u_3:=variable(matrix[1]);
u_3u_3:=assign(0);
u_1u_1:=variable(matrix[1]);
u_1u_1:=assign(0);
u_2u_2:=variable(matrix[1]);
u_2u_2:=assign(0);

u_3jc_j:=variable(matrix[1]);
u_3jc_j:=assign(0);
u_ku_k:=variable(matrix[1]);
u_ku_k:=assign(0);
u_jku_jk:=variable(matrix[1]);
u_jku_jk:=assign(0);
c_jc_j:=variable(matrix[1]);
c_jc_j:=assign(0);
u_3ku_3k:=variable(matrix[1]);
u_3ku_3k:=assign(0);
u_\alpha^2_H:=variable(matrix[1]);
u_\alpha^2_H:=assign(0);
u_\alpha^2_V:=variable(matrix[1]);
u_\alpha^2_V:=assign(0);
```

```
u_\alpha^3_H:=variable(matrix[1]);
u_\alpha^3_H:=assign(0);
u_\alpha^3_V:=variable(matrix[1]);
u_\alpha^3_V:=assign(0);
u_\alpha^4_H:=variable(matrix[1]);
u_\alpha^4_H:=assign(0);
u_\alpha^4_V:=variable(matrix[1]);
u_\alpha^4_V:=assign(0);
u_\alpha\alpha^3_H:=variable(matrix[1]);
u_\alpha\alpha^3_H:=assign(0);
u_\alpha\alpha^3_V:=variable(matrix[1]);
u_\alpha\alpha^3_V:=assign(0);

#index

North:=variable(index[1]);
South:=variable(index[1]);
Middle:=variable(index[1]);
North:=add(tnz/2,1);
#Middle:=subtract(tnz/2,1);
Middle:=assign(tnz/2);
South:=subtract(tnz/2,1);

#meanvalue_matrix

U_mean:=variable(matrix[1]);
U_mean:=meanvalue(u_vel[:,:,Middle]);
V_mean:=variable(matrix[1]);
V_mean:=meanvalue(v_vel[:,:,Middle]);
W_mean:=variable(matrix[1]);
W_mean:=meanvalue(w_vel[:,:,Middle]);
U_meanN:=variable(matrix[1]);
U_meanN:=meanvalue(u_vel[:,:,North]);
V_meanN:=variable(matrix[1]);
V_meanN:=meanvalue(v_vel[:,:,North]);
W_meanN:=variable(matrix[1]);
W_meanN:=meanvalue(w_vel[:,:,North]);
U_meanS:=variable(matrix[1]);
U_meanS:=meanvalue(u_vel[:,:,South]);
V_meanS:=variable(matrix[1]);
V_meanS:=meanvalue(v_vel[:,:,South]);
W_meanS:=variable(matrix[1]);
W_meanS:=meanvalue(w_vel[:,:,South]);

#     Densities_mean

C_mean:=variable(matrix[1]);
C_mean:=meanvalue(scal0[:,:,Middle]);
C_mean:=multiply(C_mean,2);
C_mean:=subtract(C_mean,1);
C_meanN:=variable(matrix[1]);
C_meanN:=meanvalue(scal0[:,:,North]);
C_meanN:=multiply(C_meanN,2);
C_meanN:=subtract(C_meanN,1);
```

```
C_meanS:=variable(matrix[1]);
C_meanS:=meanvalue(scal0[:,:,South]);
C_meanS:=multiply(C_meanS,2);
C_meanS:=subtract(C_meanS,1);
C_mean_3:=variable(matrix[1]);
C_mean_3:=subtract(C_meanN,C_meanS);
C_mean_3:=multiply(C_mean_3,tnz/4);

#      mean_for_calculations

mean_matrix:=variable(matrix[1]);




u_ku_k_U:=variable(matrix[tnx,tny]);
u_ku_k_U:=assign(0);
u_ku_k_V:=variable(matrix[tnx,tny]);
u_ku_k_V:=assign(0);
u_ku_k_W:=variable(matrix[tnx,tny]);
u_ku_k_W:=assign(0);
u_ku_k_U_2:=variable(matrix[tnx,tny]);
u_ku_k_U_2:=assign(0);
u_ku_k_V_2:=variable(matrix[tnx,tny]);
u_ku_k_V_2:=assign(0);
u_ku_k_W_2:=variable(matrix[tnx,tny]);
u_ku_k_W_2:=assign(0);
u_ku_k_U_3:=variable(matrix[tnx,tny]);
u_ku_k_U_3:=assign(0);
u_ku_k_V_3:=variable(matrix[tnx,tny]);
u_ku_k_V_3:=assign(0);
u_ku_k_W_3:=variable(matrix[tnx,tny]);
u_ku_k_W_3:=assign(0);
u_ku_k_U_4:=variable(matrix[tnx,tny]);
u_ku_k_U_4:=assign(0);
u_ku_k_V_4:=variable(matrix[tnx,tny]);
u_ku_k_V_4:=assign(0);
u_ku_k_W_4:=variable(matrix[tnx,tny]);
u_ku_k_W_4:=assign(0);
U_x_der:=variable(matrix[tnx,tny]);
U_x_der:=assign(0);
U_y_der:=variable(matrix[tnx,tny]);
U_y_der:=assign(0);
U_z_der:=variable(matrix[tnx,tny]);
U_z_der:=assign(0);
V_x_der:=variable(matrix[tnx,tny]);
V_x_der:=assign(0);
V_y_der:=variable(matrix[tnx,tny]);
V_y_der:=assign(0);
V_z_der:=variable(matrix[tnx,tny]);
V_z_der:=assign(0);
W_x_der:=variable(matrix[tnx,tny]);
W_x_der:=assign(0);
```

```
W_y_der:=variable(matrix[tnx,tny]);
W_y_der:=assign(0);
W_z_der:=variable(matrix[tnx,tny]);
W_z_der:=assign(0);
C_mean_x_der:=variable(matrix[tnx,tny]);
C_mean_x_der:=assign(0);
C_mean_y_der:=variable(matrix[tnx,tny]);
C_mean_y_der:=assign(0);
C_mean_z_der:=variable(matrix[tnx,tny]);
C_mean_z_der:=assign(0);
C_mean_x_der_2:=variable(matrix[tnx,tny]);
C_mean_x_der_2:=assign(0);
C_mean_y_der_2:=variable(matrix[tnx,tny]);
C_mean_y_der_2:=assign(0);
C_mean_z_der_2:=variable(matrix[tnx,tny]);
C_mean_z_der_2:=assign(0);
U_x_der_2:=variable(matrix[tnx,tny]);
U_x_der_2:=assign(0);
U_y_der_2:=variable(matrix[tnx,tny]);
U_y_der_2:=assign(0);
V_x_der_2:=variable(matrix[tnx,tny]);
V_x_der_2:=assign(0);
V_y_der_2:=variable(matrix[tnx,tny]);
V_y_der_2:=assign(0);
W_x_der_2:=variable(matrix[tnx,tny]);
W_x_der_2:=assign(0);
W_y_der_2:=variable(matrix[tnx,tny]);
W_y_der_2:=assign(0);
U_x_der_3:=variable(matrix[tnx,tny]);
U_x_der_3:=assign(0);
V_y_der_3:=variable(matrix[tnx,tny]);
V_y_der_3:=assign(0);
U_vel_dif:=variable(matrix[tnx,tny]);
U_vel_dif:=assign(0);
U_vel_dif_2:=variable(matrix[tnx,tny]);
U_vel_dif_2:=assign(0);

V_vel_dif:=variable(matrix[tnx,tny]);
V_vel_dif:=assign(0);
V_vel_dif_2:=variable(matrix[tnx,tny]);
V_vel_dif_2:=assign(0);

W_vel_dif:=variable(matrix[tnx,tny]);
W_vel_dif:=assign(0);
W_vel_dif_2:=variable(matrix[tnx,tny]);
W_vel_dif_2:=assign(0);
W_vel_dif_3:=variable(matrix[tnx,tny]);
W_vel_dif_3:=assign(0);
cc_2:=variable(matrix[tnx,tny]);
cc_2:=assign(0);
cc_3:=variable(matrix[tnx,tny]);
cc_3:=assign(0);
cc_4:=variable(matrix[tnx,tny]);
cc_4:=assign(0);
```

```
u_3c_h:=variable(matrix[tnx,tny]);
u_3c_h:=assign(0);
u_3jc_j_x:=variable(matrix[tnx,tny]);
u_3jc_j_x:=assign(0);
u_3jc_j_y:=variable(matrix[tnx,tny]);
u_3jc_j_y:=assign(0);
u_3jc_j_z:=variable(matrix[tnx,tny]);
u_3jc_j_z:=assign(0);
C_mean_dif:=variable(matrix[tnx,tny]);
C_mean_dif:=assign(0);
C_mean_dif_2:=variable(matrix[tnx,tny]);
C_mean_dif_2:=assign(0);
c_jc_j_z:=variable(matrix[tnx,tny]);
c_jc_j_z:=assign(0);
c_jc_j_z_2:=variable(matrix[tnx,tny]);
c_jc_j_z_2:=assign(0);
C_mean_x_der_22:=variable(matrix[tnx,tny]);
C_mean_x_der_22:=assign(0);
C_mean_y_der_22:=variable(matrix[tnx,tny]);
C_mean_y_der_22:=assign(0);
C_mean_z_der_22:=variable(matrix[tnx,tny]);
C_mean_z_der_22:=assign(0);


Middle_2:=variable(index[1]);
#Middle_2:=subtract(tnz/2,1);
Middle_2:=assign(tnz/2);


U_x_der:=gradient_x(u_vel[:,:,Middle_2]);
U_y_der:=gradient_y(u_vel[:,:,Middle_2]);
U_z_der:=gradient_z(u_vel[:,:,Middle_2]);
V_x_der:=gradient_x(v_vel[:,:,Middle_2]);
V_y_der:=gradient_y(v_vel[:,:,Middle_2]);
V_z_der:=gradient_z(v_vel[:,:,Middle_2]);
W_x_der:=gradient_x(w_vel[:,:,Middle_2]);
W_y_der:=gradient_y(w_vel[:,:,Middle_2]);
W_z_der:=gradient_z(w_vel[:,:,Middle_2]);
C_mean_x_der:=gradient_x(scal0[:,:,Middle_2]);
C_mean_y_der:=gradient_y(scal0[:,:,Middle_2]);
C_mean_z_der:=gradient_z(scal0[:,:,Middle_2]);
uvel:=assign(u_vel[:,:,Middle_2]);
vvel:=assign(v_vel[:,:,Middle_2]);
wvel:=assign(w_vel[:,:,Middle_2]);
scal:=assign(scal0[:,:,Middle_2]);


####################
#
label('forloop_ix');


C_mean_x_der_22:=multiply(C_mean_x_der,2);
```

```
C_mean_y_der_22:=multiply(C_mean_y_der,2);
C_mean_z_der_22:=multiply(C_mean_z_der,2);


U_x_der_2:=power(U_x_der,2);
U_y_der_2:=power(U_y_der,2);
V_x_der_2:=power(V_x_der,2);
V_y_der_2:=power(V_y_der,2);
W_x_der_2:=power(W_x_der,2);
W_y_der_2:=power(W_y_der,2);
U_x_der_3:=power(U_x_der,3);
V_y_der_3:=power(V_y_der,3);
C_mean_x_der_2:=power(C_mean_x_der_22,2);
C_mean_y_der_2:=power(C_mean_y_der_22,2);
C_mean_z_der_2:=power(C_mean_z_der_22,2);
u_ku_k_U:=subtract(uvel,U_mean);
u_ku_k_U_2:=multiply(u_ku_k_U,u_ku_k_U);
u_ku_k_U_3:=power(u_ku_k_U,3);
u_ku_k_U_4:=power(u_ku_k_U,4);
u_ku_k_V:=subtract(vvel,V_mean);
u_ku_k_V_2:=multiply(u_ku_k_V,u_ku_k_V);
u_ku_k_V_3:=power(u_ku_k_V,3);
u_ku_k_V_4:=power(u_ku_k_V,4);
u_ku_k_W:=subtract(wvel,W_mean);
u_ku_k_W_2:=multiply(u_ku_k_W,u_ku_k_W);
u_ku_k_W_3:=power(u_ku_k_W,3);
u_ku_k_W_4:=power(u_ku_k_W,4);


mean_matrix:=meanvalue(u_ku_k_U_2);
u_ku_k:=add(u_ku_k,mean_matrix);
u_\alpha^2_H:=add(u_\alpha^2_H,mean_matrix);
mean_matrix:=meanvalue(u_ku_k_U_3);
u_\alpha^3_H:=add(u_\alpha^3_H,mean_matrix);
mean_matrix:=meanvalue(u_ku_k_U_4);
u_\alpha^4_H:=add(u_\alpha^4_H,mean_matrix);
mean_matrix:=meanvalue(u_ku_k_V_2);
u_ku_k:=add(u_ku_k,mean_matrix);
u_\alpha^2_H:=add(u_\alpha^2_H,mean_matrix);
mean_matrix:=meanvalue(u_ku_k_V_3);
u_\alpha^3_H:=add(u_\alpha^3_H,mean_matrix);
mean_matrix:=meanvalue(u_ku_k_V_4);
u_\alpha^4_H:=add(u_\alpha^4_H,mean_matrix);
mean_matrix:=meanvalue(u_ku_k_W_2);
u_ku_k:=add(u_ku_k,mean_matrix);
u_\alpha^2_V:=add(u_\alpha^2_V,mean_matrix);
u_3u_3:=add(u_3u_3,mean_matrix);
#
mean_matrix:=meanvalue(u_ku_k_U_2);
u_1u_1:=add(u_1u_1,mean_matrix);
#
mean_matrix:=meanvalue(u_ku_k_V_2);
u_2u_2:=add(u_2u_2,mean_matrix);
#
```

```
mean_matrix:=meanvalue(u_ku_k_W_3);
u_\alpha^3_V:=add(u_\alpha^3_V,mean_matrix);
mean_matrix:=meanvalue(u_ku_k_W_4);
u_\alpha^4_V:=add(u_\alpha^4_V,mean_matrix);


scal:=multiply(scal,2);
scal:=subtract(scal,1);
scal:=subtract(scal,C_mean);
cc_2:=power(scal,2);
cc_3:=power(scal,3);
cc_4:=power(scal,4);
cc:=meanvalue(cc_2);
c^3:=power(scal,3);
c^4:=meanvalue(cc_4);
u_3c_h:=multiply(u_ku_k_W,scal);
u_3c:=meanvalue(u_3c_h);



mean_matrix:=meanvalue(U_x_der_2);
u_jku_jk:=add(u_jku_jk,mean_matrix);
mean_matrix:=meanvalue(U_y_der_2);
u_jku_jk:=add(u_jku_jk,mean_matrix);
mean_matrix:=meanvalue(V_x_der_2);
u_jku_jk:=add(u_jku_jk,mean_matrix);
mean_matrix:=meanvalue(V_y_der_2);
u_jku_jk:=add(u_jku_jk,mean_matrix);
mean_matrix:=meanvalue(W_x_der_2);
u_jku_jk:=add(u_jku_jk,mean_matrix);
mean_matrix:=meanvalue(W_y_der_2);
u_jku_jk:=add(u_jku_jk,mean_matrix);

mean_matrix:=meanvalue(C_mean_x_der_2);
c_jc_j:=add(c_jc_j,mean_matrix);
mean_matrix:=meanvalue(C_mean_y_der_2);
c_jc_j:=add(c_jc_j,mean_matrix);


u_3jc_j_x:=multiply(C_mean_x_der,W_x_der);
u_3jc_j_x:=multiply(u_3jc_j_x,2);
u_3jc_j_y:=multiply(C_mean_y_der,W_y_der);
u_3jc_j_y:=multiply(u_3jc_j_y,2);


mean_matrix:=meanvalue(U_x_der_3);
u_\alpha\alpha^3_H:=add(u_\alpha\alpha^3_H,mean_matrix);
mean_matrix:=meanvalue(V_y_der_3);
u_\alpha\alpha^3_H:=add(u_\alpha\alpha^3_H,mean_matrix);


U_vel_dif[0,0]:=subtract(U_meanN,U_meanS);
U_vel_dif[0,0]:=multiply(U_vel_dif[0,0],tnz/4);
```

67

```
U_vel_dif:=subtract(U_z_der,U_vel_dif[0,0]);
V_vel_dif[0,0]:=subtract(V_meanN,V_meanS);
V_vel_dif[0,0]:=multiply(V_vel_dif[0,0],tnz/4);
V_vel_dif:=subtract(V_z_der,V_vel_dif[0,0]);
W_vel_dif[0,0]:=subtract(W_meanN,W_meanS);
W_vel_dif[0,0]:=multiply(W_vel_dif[0,0],tnz/4);
W_vel_dif:=subtract(W_z_der,W_vel_dif[0,0]);

C_mean_dif[0,0]:=subtract(C_meanN,C_meanS);
C_mean_dif[0,0]:=multiply(C_mean_dif[0,0],tnz/4);
C_mean_dif:=subtract(C_mean_z_der,C_mean_dif[0,0]);
U_vel_dif_2:=power(U_vel_dif,2);
V_vel_dif_2:=power(V_vel_dif,2);
W_vel_dif_2:=power(W_vel_dif,2);


W_vel_dif_3:=power(W_vel_dif,3);

C_mean_dif_2:=power(C_mean_dif,2);
mean_matrix:=meanvalue(U_vel_dif_2);
u_jku_jk:=add(u_jku_jk,mean_matrix);
mean_matrix:=meanvalue(V_vel_dif_2);
u_jku_jk:=add(u_jku_jk,mean_matrix);
mean_matrix:=meanvalue(W_vel_dif_2);
u_jku_jk:=add(u_jku_jk,mean_matrix);

u_3ku_3k:=add(u_3ku_3k,mean_matrix);



mean_matrix:=meanvalue(W_vel_dif_3);

u_\alpha\alpha^3_V:=add(u_\alpha\alpha^3_V,mean_matrix);


u_3jc_j_z:subtract(C_mean_z_der_2,W_vel_dif);
u_3jc_j_z:=power(u_3jc_j_z,2);



mean_matrix:=meanvalue(u_3jc_j_x);
u_3jc_j:=add(u_3jc_j,mean_matrix);
mean_matrix:=meanvalue(u_3jc_j_y);
u_3jc_j:=add(u_3jc_j,mean_matrix);
mean_matrix:=meanvalue(u_3jc_j_z);
u_3jc_j:=add(u_3jc_j,mean_matrix);


c_jc_j_z:=add(C_mean_z_der,C_mean_dif);
c_jc_j_z_2:=power(c_jc_j_z,2);
mean_matrix:=meanvalue(c_jc_j_z_2);
c_jc_j:=add(c_jc_j,mean_matrix);
```

```
################
label('u_ku_k_print');

'u_ku_k':=print(u_ku_k,TIMEFORMAT);
u_\alpha^2_H:=multiply(u_\alpha^2_H,0.5);
'u_alpha^2_H':=print(u_\alpha^2_H,TIMEFORMAT);
'u_alpha^2_V':=print(u_\alpha^2_V,TIMEFORMAT);
u_\alpha^3_H:=multiply(u_\alpha^3_H,0.5);
'u_alpha^3_H':=print(u_\alpha^3_H,TIMEFORMAT);
'u_alpha^3_V':=print(u_\alpha^3_V,TIMEFORMAT);
u_\alpha^4_H:=multiply(u_\alpha^4_H,0.5);
'u_alpha^4_H':=print(u_\alpha^4_H,TIMEFORMAT);
'u_alpha^4_V':=print(u_\alpha^4_V,TIMEFORMAT);
'u_3u_3':=print(u_3u_3,TIMEFORMAT);
'u_1u_1':=print(u_1u_1,TIMEFORMAT);
'u_2u_2':=print(u_2u_2,TIMEFORMAT);
'C':=print(C_mean,TIMEFORMAT);
'C__3':=print(C_mean_3,TIMEFORMAT);
'cc':=print(cc,TIMEFORMAT);
'u_3c':=print(u_3c,TIMEFORMAT);
'c^3':=print(c^3,TIMEFORMAT);
'c^4':=print(c^4,TIMEFORMAT);
'u_jku_jk':=print(u_jku_jk,TIMEFORMAT);
u_\alpha\alpha^3_H:=multiply(u_\alpha\alpha^3_H,0.5);
'u_alphaalpha^3_H':=print(u_\alpha\alpha^3_H,TIMEFORMAT);
'u_alphaalpha^3_V':=print(u_\alpha\alpha^3_V,TIMEFORMAT);
'c_jc_j':=print(c_jc_j,TIMEFORMAT);
'u_3ku_3k':=print(u_3ku_3k,TIMEFORMAT);
'u_3jc_j':=print(u_3jc_j,TIMEFORMAT);

############
label('end');
############
end();
```

Apendix B-ii
input_postp_whole_domain.dat :

```
begin();
iz:=variable(matrix[1]);
iz:=assign(0);
uvel:=variable(matrix[tnx,tny]);
uvel:=assign(0);
vvel:=variable(matrix[tnx,tny]);
vvel:=assign(0);
wvel:=variable(matrix[tnx,tny]);
wvel:=assign(0);
scal:=variable(matrix[tnx,tny]);
scal:=assign(0);
massf:=variable(matrix[tnx,tny]);
massf:=assign(0);

###width calculations
#

label('zz1loop');
U_mean:=variable(matrix[1]);
U_mean:=meanvalue(u_vel[:,:,iz]);
V_mean:=variable(matrix[1]);
V_mean:=meanvalue(v_vel[:,:,iz]);
W_mean:=variable(matrix[1]);
W_mean:=meanvalue(w_vel[:,:,iz]);
scal:=variable(matrix[tnx,tny]);
scal:=assign(scal1[:,:,iz]);
scal:=multiply(scal,2);
scal:=add(scal,1);
C_mean:=variable(matrix[1]);
C_mean:=meanvalue(scal1[:,:,iz]);
C_mean:=multiply(C_mean,2);
C_mean:=add(C_mean,1);
end();
scal:=subtract(scal,C_mean);
uvel:=subtract(u_vel[:,:,iz],U_mean);
vvel:=subtract(v_vel[:,:,iz],V_mean);
wvel:=subtract(w_vel[:,:,iz],W_mean);
massf:=multiply(scal,wvel);
uvel:=power(uvel,2);
vvel:=power(vvel,2);
wvel:=power(wvel,2);
cc:=variable(matrix[tnz]);
cc[iz]:=meanvalue(scal[:,:]);
uc:=variable(matrix[tnz]);
uc[iz]:=meanvalue(massf[:,:]);
uu:=variable(matrix[tnz]);
uu[iz]:=meanvalue(uvel[:,:]);
vv:=variable(matrix[tnz]);
vv[iz]:=meanvalue(vvel[:,:]);
ww:=variable(matrix[tnz]);
```

70

```
ww[iz]:=meanvalue(wvel[:,:]);
iz:=add(iz,1);
if(iz,GE,tnz,'print','zz1loop');

#
label('print');
'cc_w':=print(cc,TIMEFORMAT);
'massf_w':=print(uc,TIMEFORMAT);
'uu_w':=print(uu,TIMEFORMAT);
'vv_w':=print(vv,TIMEFORMAT);
'ww_w':=print(ww,TIMEFORMAT);
############
end();
```

REFERENCES

1.   Rayleigh, L., *Investigation of the equilibrium of an incompressible heavy fluid of variable density.* Proceedings of Royal Society of London, 1884. **14**: p. 170-177.
2.   Taylor, G.I., *The instability of liquid surfaces when accelerated in a direction perpendicular to their planes I.* . Proceedings of Royal Society of London Series A, 1950. **201**: p. 192-196.
3.   Veynante, D., et al., *Gradient and counter-gradient scalar transport in turbulent premixed flames.* Journal of Fluid Mechanics, 1997 **332**: p. 263-293.
4.   Veynante, D. and L. Vervisch, *Turbulent combustion modeling.* Progress in Energy Combustion Science, 2002. **28**: p. 193-266.
5.   Britter, R.E. and S.R. Hanna, *Flow and dispersion in urban areas.* Annual Review of Fluid Mechanics, 2003. **35**: p. 469-496.
6.   Nakai, S. and H. Takabe, *Principles of inertial confinement fusion-physics of implosion and the concept of inertial fusion energy.* Report of Progress in Physics, 1996. **59**: p. 1071-1131.
7.   Lindl, J.D., *Inertial confinement fusion: the quest for ignition and energy gain using indirect drive*. 1998, Berlin: Springer.
8.   Wunsch, C. and F. R., *Vertical mixing, energy, and the general circulation of oceans.* Annual Review of Fluid Mechanics, 2004. **36**: p. 281-314.
9.   Adkins, J.F., K. McIntyre, and D.P. Schrag, *The salinity, temperature, and $\delta^{18}O$ of the glacial deep ocean.* Science, 2002. **298**: p. 1769-1773.
10.   Gull, S.F., *The X-ray, optical and radio properties of young supernova remnants.* Royal Astronomical Society Monthly Notices, 1975. **171**: p. 263-278.
11.   Colgate, S.A. and R.H. White, *The hydrodynamic behavior of supernova explosions.* Astrophysical Journal, 1966. **143**: p. 626-681.
12.   Banerjee, A. and M.J. Andrews, *3-D Simulations to investigate initial condition effects on the growth of Rayleigh-Taylor mixing.* International Journal of Heat and Mass Transfer, 2009. **52**: p. 3906-3927.
13.   Livescu, D., T. Wei, and M.R. Petersen, *Direct Numerical Simulations of Rayleigh-Taylor instability.* Journal of Physics: Conference Series, 2011. **318**(8): p. 082007.
14.   Anuchina, N.N., et al., *Turbulent mixing at an accelerating interface between liquids of different densities.* Fluid Dynamics, 1978. **13**(6): p. 916-920.
15.   Youngs, D.L., *Numerical simulation of turbulent mixing by Rayleigh-Taylor instability.* Physica D, 1984. **12**: p. 32-44.
16.   Wei, T. and D. Livescu, *Late-time quadratic growth in single-mode Rayleigh-Taylor instability.* Physical Review E, 2012. **86**(4): p. 046405.
17.   Ramaprabhu, P. and M.J. Andrews, *On the initialization of Rayleigh-Taylor simulations.* Physics of Fluids, 2004. **16**: p. L59-L62.
18.   Ramaprabhu, P., G. Dimonte, and M.J. Andrews, *A numerical study of the influence of initial perturbations on the turbulent Rayleigh-Taylor instability.* Journal of Fluid Mechanics, 2005. **536**: p. 285-319.

19.	Dimonte, G., *Dependence of turbulent Rayleigh-Taylor instability on initial perturbations.* Physical Review E, 2004. **69**(5): p. 056305.

20.	Banerjee, A., W.N. Kraft, and M.J. Andrews, *Detailed measurements of a Rayleigh-Taylor mixing layer from small to intermediate Atwood Numbers.* Journal of Fluid Mechanics, 2010. **659**: p. 129-190.

21.	Ramaprabhu, P. and M.J. Andrews, *Experimental investigation of Rayleigh- Taylor mixing at small Atwood numbers.* Journal of Fluid Mechanics, 2004. **502**: p. 233-271.

22.	Dimonte, G., et al., *A comparative study of the turbulent Rayleigh-Taylor (RT) instability using high-resolution 3D numerical simulations: The Alpha-Group collaboration,.* Physics of Fluids, 2004. **16**: p. 1668-1693.

23.	Dimonte, G., P. Ramaprabhu, and M.J. Andrews, *Rayleigh-Taylor instability with complex acceleration history.* Physical Review E, 2007. **76**: p. 046313.

24.	Livescu, D. and T. Wei, *Direct Numerical Simulations of Rayleigh-Taylor instability with gravity reversal.* Seventh International Computationl Fluid Dynamics (ICCFD7), 2012: p. 9-13.

25.	Ramaprabhu, P., V. Karkhanis, and A.G.W. Lawrie, *The Rayleigh-Taylor Instability driven by an accel-decel-accel profile.* Physics of Fluids (1994-present), 2013. **25**(11): p. -.

26.	Dimonte, G. and M. Schneider, *Turbulent Rayleigh-Taylor instability experiments with variable acceleration.* Physical Review E, 1996. **54**: p. 3740-3743.

27.	Lawrie, A.G.W., *On Rayleigh-Taylor mixing: confinement by stratification and geometry*. 2009, University of Cambridge.

28.	Lawrie, A.G.W. and S.B. Dalziel, *Turbulent diffusion in tall tubes. I. Models for Rayleigh-Taylor instability.* Physics of Fluids (1994-present), 2011. **23**(8): p. -.

29.	Lawrie, A.G.W. and S.B. Dalziel, *Turbulent diffusion in tall tubes. II. Confinement by stratification.* Physics of Fluids (1994-present), 2011. **23**(8): p. -.

30.	Strang, G., *On the Construction and Comparison of Difference Schemes.* SIAM Journal on Numerical Analysis, 1968. **5**(3): p. 506-517.

31.	RAMAPRABHU, P. and M.J. ANDREWS, *Experimental investigation of Rayleigh–Taylor mixing at small Atwood numbers.* Journal of Fluid Mechanics, 2004. **502**: p. 233-271.

32.	MUESCHKE, N.J., M.J. ANDREWS, and O. SCHILLING, *Experimental characterization of initial conditions and spatio-temporal evolution of a small-Atwood-number Rayleigh–Taylor mixing layer.* Journal of Fluid Mechanics, 2006. **567**: p. 27-63.

33.	Cabot, W.H. and A.W. Cook, *Reynolds number effects on Rayleigh-Taylor instability with possible implications for type-Ia supernovae.* Nature Physics, 2006. **2**: p. 562-568.

34.	Young, Y.N., et al., *On the miscible Rayleigh-Taylor instability: two and three dimensions.* Journal of Fluid Mechanics, 2001. **447**: p. 377-408.

35.	LLOR, A., *Bulk turbulent transport and structure in Rayleigh–Taylor, Richtmyer–Meshkov, and variable acceleration instabilities.* Laser and Particle Beams, 2003. **21**(03): p. 305-310.

36.	Poujade, O. and M. Peybernes, *Growth rate of Rayleigh-Taylor turbulent mixing layers with the foliation approach.* Phys Rev E Stat Nonlin Soft Matter Phys, 2010. **81**(1 Pt 2): p. 26.

37.   Gréa, B.-J., *The rapid acceleration model and the growth rate of a turbulent mixing zone induced by Rayleigh-Taylor instability.* Physics of Fluids (1994-present), 2013. **25**(1): p. - .

38.   Mikaelian, K.O., *Analytic approach to nonlinear hydrodynamic instabilities driven by time-dependent accelerations.* Physical Review E, 2010. **81**(1): p. 016325.

39.   Haan, S.W., *Onset of nonlinear saturation for Rayleigh-Taylor growth in the presence of a full spectrum of modes.* Physical Review A, 1989. **39**(11): p. 5812-5825.

40.   Ristorcelli, J.R. and T.T. Clark, *Rayleigh-Taylor turbulence: self-similar analysis and direct numerical simulations. .* Journal of Fluid Mechanics, 2004. **507**: p. 213-253.

41.   Andrews, M.J., *Accurate Computation of Convective Transport in Transient Two-Phase Flow.* International Journal for Numerical Methods in Fluids 1995. **21**(3): p. 205-222.

42.   Dimonte, G. and M. Schneider, *Density ratio dependence of Rayleigh-Taylor mixing for sustained and impulsive acceleration histories.* Physics of Fluids, 2000. **12**: p. 304-321.

43.   Livescu, D. and J.R. Ristorcelli, *Buoyancy-driven variable density turbulence.* Journal of Fluid Mechanics, 2007. **591**: p. 43-71.

44.   Cook, A.W., W. Cabot, and P.L. Miller, *The mixing-transition in Rayleigh-Taylor instability.* Journal of Fluid Mechanics, 2004. **511**: p. 333-362.

45.   LIVESCU, D. and J.R. RISTORCELLI, *Variable-density mixing in buoyancy-driven turbulence.* Journal of Fluid Mechanics, 2008. **605**: p. 145-180.

VITA

Denis Aslangil was born on April 7th, 1989 in Istanbul, Turkey. He earned his bachelor's degrees in both mechanical engineering and industrial engineering (double major) from the Istanbul Technical University. He attended Lehigh University, Mechanical Engineering and Mechanics Department in the Fall 2012 to pursue MSc and PhD degrees in Mechanical Engineering. He joined to Turbulent Flow Design Group in January 2013; and currently, he is a PhD student under Prof. Arindam Banerjee's guidance at Lehigh University.